8

ANISOTROPIES

The primordial perturbations set up during inflation manifest themselves in the radiation as well as in the matter distribution. By understanding the evolution of the photon perturbations, we can make predictions about the expected anisotropy spectrum today. This evolution is again completely determined by the Einstein–Boltzmann equation we derived in Chapters 4 and 5, and one way to go would be to simply stick all the relevant equations in those chapters on a computer and solve them numerically. Historically, this is a pretty good caricature of what happened. Long before we developed deep insight into the physics of anisotropies, various groups had codes which determined the expected spectra from different models. Only much later did we come to understand both qualitatively and quantitatively why the spectra look like they do.[1] In this chapter, I will mangle the history and simply explain what we have learned about the physics of anisotropies.

Perturbations to the photons evolved completely differently before and after the epoch of recombination at $z \simeq 1100$. Before recombination, the photons were tightly coupled to the electrons and protons; all together they can be described as a single fluid (dubbed the "baryon–photon" fluid). After recombination, photons free-streamed from the "surface of last scattering" to us today. After an overview which qualitatively explains the anisotropy spectrum, Sections 8.2–8.4 work through the physics of the baryon-photon fluid before recombination. Then Sections 8.5–8.6 treat the post-recombination era, culminating in the predicted spectrum of anisotropies today. Finally Section 8.7 discusses how these spectra vary when the cosmological parameters change.

---

[1] Understanding the anisotropies actually helped make the codes much more efficient. The prime example of this is the popular code CMBFAST (Seljak and Zaldarriaga, 1996) which is based in part on the analytic solution presented in this chapter.

8.1 OVERVIEW

Let's begin as we did in the last chapter, by cheating and looking at the answers first. Figure 8.1 shows the evolution of the perturbations to the photons. Four Fourier modes corresponding to perturbations on four different scales are shown. Qualitatively, the most important feature of Figure 8.1 is that perturbations to the photons do not grow appreciably with time. This stands in stark contrast to the matter perturbations, which do grow. And this contrast is something we should have expected: the pressure of the photons is so large that it can withstand the tendency toward collapse. This means that the small perturbations set up during inflation stay small; they remain linear all the way up to the present.

Before going further and examining the evolution of the different modes in more detail, a technical note: I have plotted not simply the perturbation to the photons but rather the combination $k^{3/2}(\Theta_0 + \Psi)$. The $k^{3/2}$ factor balances the fact that the amplitude of the perturbations (in a simple inflationary model) scales as $k^{-3/2}$. I have added the gravitational potential Ψ because the photons we see today had to travel out of the potentials they were in at the time of recombination. As they emerged from these potential wells, their wavelengths were stretched (if the region was overdense and $\Psi < 0$), thereby decreasing their energy. Thus, the temperature we see today is actually Θ_0 at recombination plus Ψ.

The large-scale mode in Figure 8.1 evolves hardly at all. This is not surprising: no causal physics can affect perturbations with wavelengths larger than the horizon, so a super-horizon mode should exhibit little evolution. This means that when we observe large-scale anisotropies — which are sensitive to modes with wavelengths larger than the horizon at recombination — we are observing perturbations in their most pristine form, as they were set down at very early times, presumably during inflation.

Figure 8.1 shows that the smaller scale modes evolve in a more complicated way than the super-horizon modes. Consider the curve labeled "First Peak." As the mode enters the horizon, the perturbation begins to grow until it reaches an apparent maximum at the time of recombination. If we observe anisotropies on scales corresponding to this mode, we would expect to see large fluctuations. Hence the label: the anisotropy spectrum will have a peak at the angular scales corresponding to the mode which has just reached its peak at recombination.

The mode in Figure 8.1 which enters the horizon slightly earlier peaks earlier and then turns over so that its amplitude at recombination is zero. By recombination, it has undergone half of an oscillation; so we see our first clear signal of the *acoustic oscillations* due to the pressure of the relativistic photons. The phase of this mode is such that, at recombination its amplitude is zero. Therefore, when we observe anistropies today corresponding to these scales, we expect very small fluctuations. There will be a trough in the anisotropy spectrum on these angular scales.

And on it goes. The curve labeled "Second Peak" entered the horizon even earlier and has gone through one full oscillation by recombination. As such, this mode will have large fluctuations and lead to a second peak in the anisotropy spectrum. You
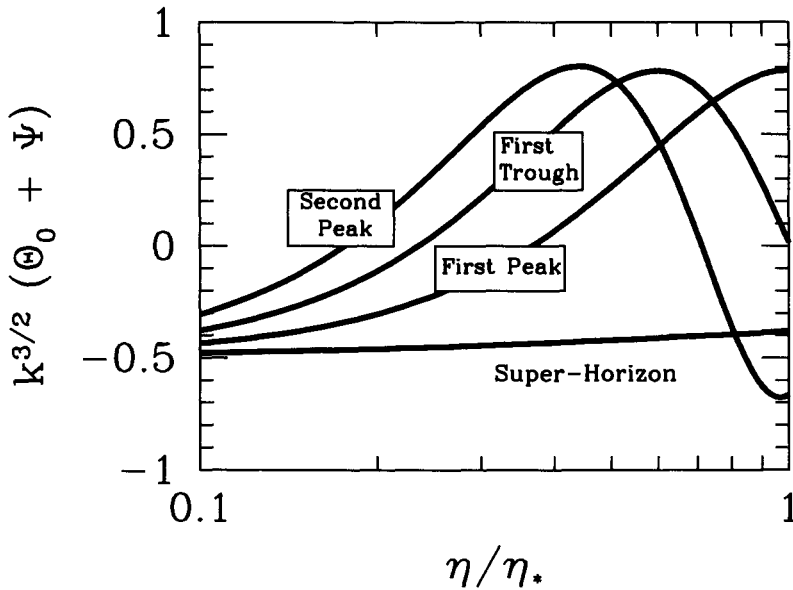
Figure 8.1. Evolution of photon perturbations of four different modes before recombination at η_*. Normalization is arbitrary, but the relative normalization of the 4 curves is appropriate for perturbations with a Harrison–Zel'dovich–Peebles ($n = 1$) spectrum. Model is standard CDM with $h = 0.5$, $\Omega_m = 1$, and $\Omega_b = 0.06$. Starting from the bottom left and moving upward, the wavenumbers for the modes are $k = (7 \times 10^{-4}, 0.022, 0.034, 0.045)$ Mpc^{-1} or $(8, 260, 400, 540)/\eta_0$.

might expect that there will be a never-ending series of peaks and troughs in the anisotropy spectrum corresponding to modes that entered the horizon earlier and earlier. And you would be right: this is exactly what happens.

We can see this more clearly by looking at the spectrum of perturbations at one time, the time of recombination. Figure 8.2 shows this spectrum for two different models, one with a very low baryon content. We do indeed see this pattern of peaks and troughs. There are two more quantitative features of these oscillations that are important. First, note that — at least in the higher baryon model — the heights of the peaks seem to alternate: the odd peaks seem higher than the even peaks. Second, and this is clearest in the low baryon model, perturbations on small scales $k\eta_0 \gtrsim 500$ are damped.

To understand the first of these features, we can write down a cartoon version of the equation governing perturbations. Very roughly, this equation is

$$\ddot{\Theta}_0 + k^2 c_s^2 \Theta_0 = F \tag{8.1}$$

where F is a driving force due to gravity and c_s is the sound speed of the combined baryon–photon fluid. This is the equation of a forced harmonic oscillator (see box on page 220). Qualitatively, it predicts the oscillations we have seen above. But it also
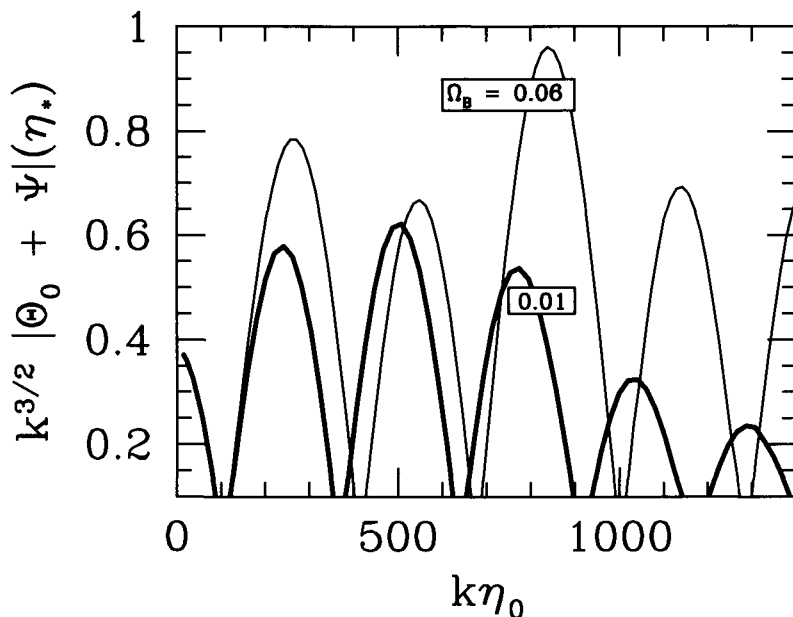
Figure 8.2. Perturbations to the photon distribution at recombination in two models. The larger damping length of the low-Ω_b model is clearly evident in the suppression of perturbations for modes with $k > 500/\eta_0$.

explains something about the heights of the peaks. As we add more baryons to the universe, the sound speed goes down (baryons are heavy so they reduce the speed). Thus the frequency of the oscillations goes down. The peaks at $n\pi/\omega$ are shifted to larger k (you really should read that box!), and the spacing between peaks gets correspondingly larger. Further, as the frequency goes down, the disparity between the heights of the odd and even peaks gets larger. We clearly see both of these features in Figure 8.2. Another way of understanding the alternating peak heights is to note that the perturbations for the first peak mode have been growing since they entered the horizon. By decreasing the pressure (or equivalently increasing the importance of gravity) these modes will grow even more. The second peak mode on the other hand, corresponds to an *underdensity* of photons in the potential wells. Decreasing the pressure makes it harder for photons to escape the well and therefore reduces the magnitude of the perturbation (makes it less underdense).

Consider a simple harmonic oscillator with mass m and force constant k. In addition to the restoring force, the oscillator is acted on by an external force F_0. Thus the full force is $F_0 - kx$ where x is the oscillator's position. The equation of motion is

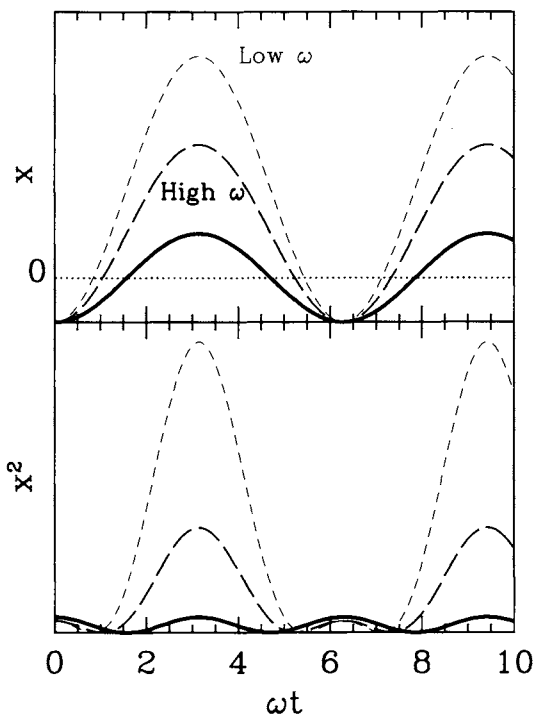$$\ddot{x} + \frac{k}{m}x = \frac{F_0}{m}. \tag{8.2}$$

The term on the right-hand side — representing the external force — is driving the oscillator to large values of x. The restoring force on the other hand tries to keep the oscillator as close to the origin as possible. The solution therefore will be that oscillations will be set up around a new zero point, at positive x.

The solution to Eq. (8.2) is the sum of the general solution to the homogeneous equation (with the right-hand side set to zero) and a particular solution. The general solution has two modes, best expressed as a sine and cosine with arguments ωt, with the frequency ω defined as $\omega \equiv \sqrt{\frac{k}{m}}$. A particular solution to Eq. (8.2) is constant $x = F_0/m\omega^2$, so the full solution is the sum of the sine and cosine modes plus this constant. Let us assume that the oscillator is initially at rest. Then, since $\dot{x}(0)$ is proportional to the coefficient of the sine mode, this coefficient must vanish, leaving

$$x = A\cos(\omega t) + \frac{F_0}{m\omega^2}. \tag{8.3}$$

This solution is shown in the figure at right. The solid line is the unforced solution: oscillations about the origin. The dashed curves are the forced solutions for two different choices of frequencies. In both cases, the oscillations are not around $x = 0$ as they would be if the system was unforced. Once an external force is introduced, the zero point of the oscillations shifts in the direction of the force. Two curves are drawn to show that this shift is more dramatic for lower frequencies. The bottom panel shows the square of the oscillator position as a function of time. All three oscillators experience a series of peaks at $t = n\pi/\omega$ corresponding to the minima/maxima of the cosine mode. (Note that if only the sine mode was present these peaks would be at $t = (2n + 1)\pi/\omega$.) The heights of these peaks are identical in the case of the unforced oscillator and equal to the height at $t = 0$. In the forced case, though, the height of the odd peaks — those at $t = (2n + 1)\pi/\omega$ — is greater than that of the even peaks. The effect is most dramatic for low frequencies. If the frequency is low, the force has a greater effect, producing the greater zero-point offset, and hence the greater odd/even disparity. The other feature of this example is that the even peaks correspond to negative positions of the oscillator: points at which it is farthest from where the force wants it to go.

Forced Harmonic Oscillator
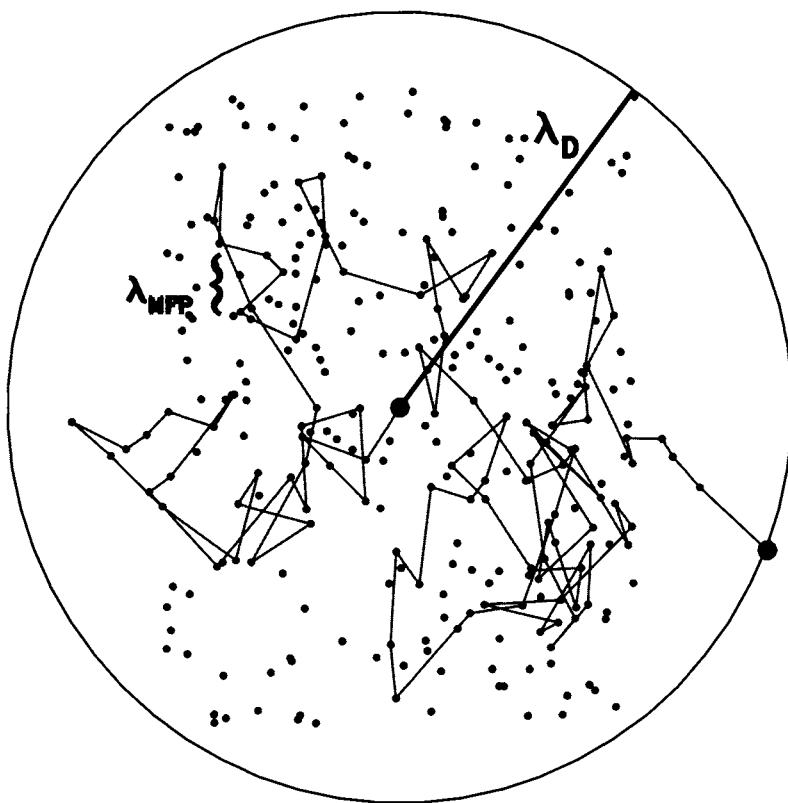
Photon Diffusion

Figure 8.3. Photon diffusion through the electron gas. Electrons are denoted as points. Shown is a typical photon path as it scatters off electrons. The mean free path is λ_{MFP}. After a Hubble time, the photon has scattered many times, so that it has moved a distance of order λ_D.

To understand the damping evident in Figure 8.2, we need to remember that the approximation of the photons and electrons and baryons moving together as a single fluid is just that, an approximation. It is valid only if the scattering rate of photons off of electrons is infinite. Of course this condition is not met: photons travel a finite distance in between scatters. Consider Figure 8.3, which depicts the path of a single photon as it scatters off a sea of electrons. It travels a mean distance λ_{MFP} in between each scatter. In our case this distance is $(n_e \sigma_T)^{-1}$. If the density of electrons is very large, then the mean free path is correspondingly small. In the course of a Hubble time, H^{-1}, a photon scatters of order $n_e \sigma_T H^{-1}$ times (simply the product of the rate and the time). As depicted in Figure 8.3, each scatter contributes to the random walk of the photon. We know that the total distance traveled in the course of a random walk is the mean free path times the square

root of the total number of steps. Therefore, a cosmological photon moves a mean distance

$$\lambda_D \sim \lambda_{\text{MFP}} \sqrt{n_e \sigma_T H^{-1}}$$

$$= \frac{1}{\sqrt{n_e \sigma_T H}} \tag{8.4}$$

in a Hubble time. Any perturbation on scales smaller than λ_D can be expected to be washed out. In Fourier space this will correspond to damping of all high k-modes. Note that this crude estimate gets the Ω_b dependence right. Models with small baryon density have a larger λ_D (since n_e is proportional to Ω_b when the universe is ionized). Therefore, the damping sets in at larger scales, or smaller k. This is precisely what we saw in Figure 8.2.

The final step is to relate the perturbations at recombination, as depicted in Figure 8.2, to the anisotropies we observe today. The math of this is a little complicated, but the physics is perfectly straightforward. Consider one Fourier mode, a plane-wave perturbation. Figure 8.4 shows the temperature variations for one mode at recombination. Photons from hot and cold spots separated by a typical (comoving) distance k^{-1} travel to us coming from an angular separation $\theta \simeq k^{-1}/(\eta_0 - \eta_*)$ where $\eta_0 - \eta_*$ is the (comoving) distance between us and the surface of last scattering.[2] If we decompose the temperature field into multipole moments, then an angular scale θ roughly corresponds to $1/l$. So, using the fact that $\eta_* \ll \eta_0$, we project inhomogeneities on scales k onto anisotropies on angular scales $l \simeq k\eta_0$.

There is one final caveat to this picture of free-streaming. We have been implicitly assuming that nothing happens to the photons on their journey from the last scattering surface to Earth. In fact, if the universe was flat and matter dominated through this whole time, then gravitational potentials remain constant, and this assumption is correct. However, recombination takes places not too much later than the epoch of equality, so the remnant radiation density means potentials are not exactly constant right after recombination. Also, at late times, dark energy does not behave like matter and leads to potential decay. You can imagine other disruptions to matter domination. All of these so-called *integrated Sachs–Wolfe effects* produce new perturbations to the photons, leading to changes typically of order 10%.

And that's it; we now understand how primordial perturbations are processed to form the present-day anisotropy spectrum. Let's work through it again quantitatively.

8.2 LARGE-SCALE ANISOTROPIES

To find the large-scale solution for the photon perturbation, we make use of the super-horizon equation, (7.17). This immediately tells us that $\Theta_0 = -\Phi$ plus a

---

[2]This is true only in a flat universe. In an open universe, the distance to the last scattering surface is larger, so the same physical scale is projected onto a smaller angular scale.
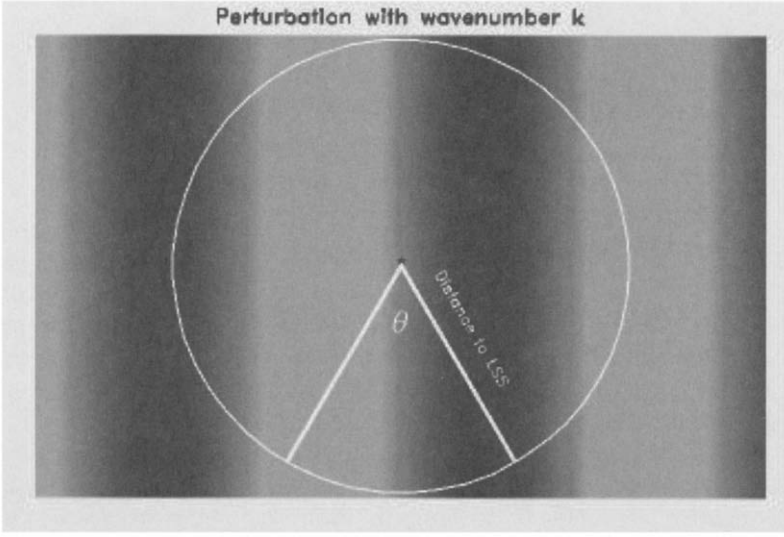
Figure 8.4. Free-streaming. Perturbations in the temperature at recombination from one plave wave with wavenumber k. Hot and cold spots are shaded light and dark. After recombination, photons from the hot and cold spots travel freely to us, here denoted by the star at the center. This mode contributes anisotropy on a scale $\theta \sim k^{-1}/$(Distance to last scattering surface).

constant. The initial conditions are such that $\Theta_0 = \Phi/2$, so the constant is $3\Phi_{\rm p}/2$, where $\Phi_{\rm p}$ is the primordial potential set up during inflation. We have an exact expression for the large-scale evolution of Φ, Eq. (7.32). If recombination takes place long after the epoch of equality, then we can take the $y \gg 1$ limit of this expression, $\Phi \to 9\Phi_{\rm p}/10$. Therefore, at recombination, large-scale photon perturbations satisfy

$$\Theta_0(k,\eta_*) = -\Phi(k,\eta_*) + \frac{3\Phi_{\rm p}(k)}{2}$$

$$= \frac{2\Phi(k,\eta_*)}{3}. \tag{8.5}$$

The observed anisotropy is $\Theta_0 + \Psi$, which to a good approximation is $\Theta_0 - \Phi$ since $\Psi \simeq -\Phi$. Therefore,

$$(\Theta_0 + \Psi)(k,\eta_*) = \frac{1}{3}\Psi(k,\eta_*). \tag{8.6}$$

Another useful way of expressing the large-scale perturbations at recombination is in terms of the density field. The initial conditions derived in Chapter 6 were that $\delta = 3\Phi/2$. Integrating the large-scale evolution equation, $\dot{\delta} = -3\dot{\Phi}$, leads to

$$\delta(\eta_*) = \frac{3}{2}\Phi_{\rm p} - 3[\Phi(\eta_*) - \Phi_{\rm p}]$$

$$= 2\Phi(\eta_*). \tag{8.7}$$

So the observed anisotropy expressed in terms of the dark matter overdensity is

$$(\Theta_0 + \Psi)(k, \eta_*) = -\frac{1}{6}\delta(\eta_*). \tag{8.8}$$

Equations (8.6) and (8.8) will be useful to us when we compute the large-scale anisotropy spectrum. However, even now, they contain a fascinating piece of information. From the Fourier transform of Eq. (8.8), we see that the observed anisotropy of an overdense region will be *negative*. This is such a surprising result that it is worth repeating. For large-scale perturbations, overdense regions do indeed contain hotter photons at recombination than do underdense regions: i.e., $\Theta_0 > 0$ when $\Psi < 0$. However, to get to us today, these photons must travel out of their potential wells. In so doing they lose energy, and this energy loss more than compensates for the fact that the photons were initially hotter than average: i.e., $\Theta_0 + \Psi$ is negative when $\Psi < 0$. To sum up, when we observe large-scale hot spots on the sky today, we are actually observing regions that were underdense at the time of recombination.

The other important feature of Eq. (8.8) is the coefficient $1/6$. It enables us to relate "$\delta T/T$" (the left-hand side) to "$\delta\rho/\rho$" (the right). Very roughly speaking, an anisotropy of order 10^{-5} corresponds to an overdensity of 6×10^{-5}. One of the important questions which must be addressed by the picture of gravitational instability is whether the observed anisotropy is consistent with the overdensities needed to form structure by today. This factor of 6 is a huge help. In almost all models of structure formation other than inflation, this factor of 6 is replaced by a number much closer to unity (see Exercise 1 for a specific example). Therefore, they struggle with the fact that the observed level of anisotropy is too small to account for the clustering of matter in the universe. Equivalently, when normalized to large-angle anisotropies, the matter power spectrum is too small.[3]

8.3 ACOUSTIC OSCILLATIONS

8.3.1 Tightly Coupled Limit of the Boltzmann Equations

When all electrons were ionized, before η_*, the mean free path for a photon was much smaller than the horizon of the universe. Compton scattering caused the electron–proton fluid to be tightly coupled with the photons. We now proceed to explore this regime quantitatively using the Boltzmann equations.

The tightly coupled limit corresponds to the scattering rate being much larger than the expansion rate: $\tau \gg 1$, where τ is the optical depth defined in Eq. (4.61). I

---

[3]This realization has been most important in theories in which structure is generated by cosmic strings. Several papers which pointed out the problem in the aftermath of the COBE detection include: Albrecht and Stebbins (1992), Perivolaropoulos and Vachaspati (1994), and Pen and Spergel (1995).

want to argue that in the $\tau \gg 1$ limit, the only nonnegligible moments, Θ_l, are the monopole ($l = 0$) and the dipole ($l = 1$). All others are suppressed. In this sense, photons behave just like a fluid, which can be described with only two variables: the density ρ and the velocity $\vec{v}$. In order to show this, let's go back to the Boltzmann equation (4.100) for photons. We want to turn this differential equation for $\Theta(\eta, \mu)$ into an infinite set of coupled equations for $\Theta_l(\eta)$. The advantage is that — as we will see — the higher moments are small and so can be neglected. The strategy is to multiply by $\mathcal{P}_l(\mu)$ and then integrate over μ. Using Eq. (4.99), the Boltzmann equation for $l > 2$ becomes

$$\dot{\Theta}_l + \frac{k}{(-i)^{l+1}} \int_{-1}^{1} \frac{d\mu}{2} \mu \mathcal{P}_l(\mu) \Theta(\mu) = \dot{\tau} \Theta_l. \tag{8.9}$$

Note that all other terms (e.g., $-\dot{\Phi}$) have simple μ dependence (scale as μ^0 or μ^1) so all $l > 2$ moments vanish for them. To do the integral, we make use of the recurrence relation for Legendre polynomials, Eq. (C.3), to get

$$\dot{\Theta}_l - \frac{kl}{2l+1} \Theta_{l-1} + \frac{k(l+1)}{2l+1} \Theta_{l+1} = \dot{\tau} \Theta_l. \tag{8.10}$$

Let us consider the order of magnitude of the terms in Eq. (8.10). The first term on the left is of order Θ_l/η which is much smaller than the term on the right which is of order $\tau \Theta_l/\eta$. Neglecting the Θ_{l+1} term for the moment, this tells us that in the tightly coupled regime

$$\Theta_l \sim \frac{k\eta}{2\tau} \Theta_{l-1}. \tag{8.11}$$

For horizon size modes $k\eta \sim 1$, this means that $\Theta_l \ll \Theta_{l-1}$. (By the way, this is justification for throwing out the Θ_{l+1} term in making our estimate.) This estimate is valid for all modes higher than the dipole, so all such modes are very small compared to the monopole and dipole.

Before making use of this fact and deriving the tightly coupled equations in the limit in which only the monopole and dipole are nonzero (the fluid approximation), I want to explain *why* higher moments are damped in a tightly coupled environment. Indeed this observation is extremely important not only in cosmology but in all settings in which the fluid approximation is used. To understand the fluid approximation, consider one plane-wave perturbation as depicted in Figure 8.5. An observer sitting at the center of the perturbation sees photons arriving from a distance of order the mean free path, η/τ. A wavelength of order the horizon η is much larger than this distance, so the photons arriving at the observer all have the same temperature. There is very little anisotropy. You might think that a perturbation with a very small wavelength (with $k\eta \sim \tau$) would lead to anisotropy. In fact, though, such a mode has a wavelength much smaller than the damping scale. So all perturbations on such small scales are smoothed out, again leading to no anisotropy. The bottom line is there is essentially no anisotropy beyond the monopole and the dipole in the tightly coupled regime.

Tightly Coupled Limit

Figure 8.5. Anisotropies in the tightly coupled era. Perturbations on the scale of the horizon cannot be observed by an observer [denoted by the star here], for the photons observed come from the last scattering surface a distance η/τ away. This last scattering surface is so close that photons arriving from all angles have virtually identical temperatures.

Armed with this knowledge, we can now turn to the equations for the first two moments, which — after disposing of Θ_2 — read:

$$\dot{\Theta}_0 + k\Theta_1 = -\dot{\Phi} \tag{8.12}$$

$$\dot{\Theta}_1 - \frac{k\Theta_0}{3} = \frac{k\Psi}{3} + \dot{\tau}\left[\Theta_1 - \frac{iv_b}{3}\right]. \tag{8.13}$$

These follow by mutiplying Eq. (4.100) by $\mathcal{P}_0(\mu)$ and $\mathcal{P}_1(\mu)$ and integrating over μ. They are supplemented by the equations for the electron–baryon fluid, Eqs. (4.105) and (4.106). Let us first rewrite the velocity equation, (4.106), as

$$v_b = -3i\Theta_1 + \frac{R}{\dot{\tau}}\left[\dot{v}_b + \frac{\dot{a}}{a}v_b + ik\Psi\right]. \tag{8.14}$$

The second term on the right here is much smaller than the first since it is suppressed by a relative factor of order τ^{-1}. Thus, to lowest order, $v_b = -3i\Theta_1$. A systematic way to expand, then, is to use this lowest order expression everywhere in the second term, leading to

$$v_b \simeq -3i\Theta_1 + \frac{R}{\dot{\tau}}\left[-3i\dot{\Theta}_1 - 3i\frac{\dot{a}}{a}\Theta_1 + ik\Psi\right]. \tag{8.15}$$

Now let us insert this expression into Eq. (8.13), eliminating v_b. After rearranging terms, we find

$$\dot{\Theta}_1 + \frac{\dot{a}}{a}\frac{R}{1+R}\Theta_1 - \frac{k}{3[1+R]}\Theta_0 = \frac{k\Psi}{3}. \tag{8.16}$$

We now have two first-order coupled equations for the first two photon moments, Eqs. (8.12) and (8.16). We can turn these into one second-order equation by differentiating Eq. (8.12) and using Eq. (8.16) to eliminate $\dot{\Theta}_1$:

$$\ddot{\Theta}_0 + k\left[\frac{k\Psi}{3} - \frac{\dot{a}}{a}\frac{R}{1+R}\Theta_1 + \frac{k}{3[1+R]}\Theta_0\right] = -\ddot{\Phi}. \tag{8.17}$$

Finally, we use Eq. (8.12) to eliminate Θ_1 here. This leaves

$$\ddot{\Theta}_0 + \frac{\dot{a}}{a}\frac{R}{1+R}\dot{\Theta}_0 + k^2 c_s^2 \Theta_0 = -\frac{k^2}{3}\Psi - \frac{\dot{a}}{a}\frac{R}{1+R}\dot{\Phi} - \ddot{\Phi} \equiv F(k,\eta) \tag{8.18}$$

where I have defined the forcing function on the right as F and the sound speed of the fluid as

$$c_s \equiv \sqrt{\frac{1}{3(1+R)}}. \tag{8.19}$$

The sound speed depends on the baryon density in the universe. In the absence of baryons, it has the standard value for a relativistic fluid, $c_s = 1/\sqrt{3}$. The presence of baryons, though, makes the fluid heavier, thereby lowering the sound speed. We will see shortly that the fluid oscillates in both space and time, with a period which is determined by the sound speed, and hence by the baryon density. Note that Eq. (8.18) is the "grown-up" version of Eq. (8.1); it differs only through the $\dot{\Theta}_0$ damping[4] term (see Exercise 2). The presence of this term does not change any of the qualitiative conlcusions we reached in Section 8.1. Finally, note that Φ enters on the right in a very similar way as Θ_0 does on the left. An alternate version of Eq. (8.18) takes adavantage of this:

$$\left\{\frac{d^2}{d\eta^2} + \frac{\dot{R}}{1+R}\frac{d}{d\eta} + k^2 c_s^2\right\}[\Theta_0 + \Phi] = \frac{k^2}{3}\left[\frac{1}{1+R}\Phi - \Psi\right]. \tag{8.20}$$

8.3.2 Tightly Coupled Solutions

The equation we have derived governing acoustic oscillations of the photon–baryon fluid, (8.20), is a second-order ordinary differential equation. To solve it, we will again (as in Section 7.3.1) use Green's method to find the full solution. First we find the two solutions to the homogeneous equation. Then we use these to construct the particular solution.

In prnciple, to obtain the homogeneous solutions, we must solve the damped, harmonic oscillator equation, (8.20) with the right-hand side equal to zero. In practice, the damping term is of order $R(\Theta_0 + \Phi)/\eta^2$ while the pressure term is much

---

[4]This "damping" term is not to be confused with the damping of perturbations on small scales treated in the next section. They are completely different effects.

larger, of order $k^2 c_s^2 (\Theta_0 + \Phi)$ (at least it's larger when modes are within the horizon or when R is small). Physically we expect pressure to induce oscillations in the photon temperature; the time scale for these oscillations is much shorter than the damping introduced by the expansion of the universe. To a first approximation, then, let us neglect the damping term and simply obtain the oscillating solutions.[5] In this limit, the two homogeneous solutions are

$$S_1(k, \eta) = \sin\left[kr_s(\eta)\right] \qquad ; \qquad S_2(k, \eta) = \cos\left[kr_s(\eta)\right] \qquad (8.21)$$

where I have defined the *sound horizon* as

$$r_s(\eta) \equiv \int_0^\eta d\eta' c_s(\eta'). \qquad (8.22)$$

Since c_s is the sound speed, the sound horizon is the comoving distance traveled by a sound wave by time η.

The tightly coupled solution for the photon temperature can be constructed from the homogeneous solutions of Eq. (8.21):

$$\Theta_0(\eta) + \Phi(\eta) = C_1 S_1(\eta) + C_2 S_2(\eta)$$

$$+ \frac{k^2}{3} \int_0^\eta d\eta' \left[\Phi(\eta') - \Psi(\eta')\right] \frac{S_1(\eta')S_2(\eta) - S_1(\eta)S_2(\eta')}{S_1(\eta')\dot{S}_2(\eta') - \dot{S}_1(\eta')S_2(\eta')}. \qquad (8.23)$$

Here again, I have dropped all occurences of R except in the arguments of the rapidly varying sines and cosines. That is, the argument of S_1, for example, is still taken to be kr_s with its nonzero value of R. We can fix the constants C_1 and C_2 in Eq. (8.23) by appealing to the initial conditions, when both Θ_0 and Φ are constants. The coefficient of the sine term therefore, C_1, must vanish, and $C_2 = \Theta_0(0) + \Phi(0)$. The denominator in the integrand reduces to $-kc_s(\eta') \to -k/\sqrt{3}$ in the limit in which we are working. Finally, the difference of the products in the numerator of the integrand is simply $-\sin[k(r_s - r_s')]$, so

$$\Theta_0(\eta) + \Phi(\eta) = \left[\Theta_0(0) + \Phi(0)\right] \cos(kr_s)$$

$$+ \frac{k}{\sqrt{3}} \int_0^\eta d\eta' \left[\Phi(\eta') - \Psi(\eta')\right] \sin\left[k(r_s(\eta) - r_s(\eta'))\right]. \qquad (8.24)$$

Equation (8.24) is an expression for the anisotropy in the tightly coupled limit, first derived by Hu and Sugiyama in 1995. If you are not impressed with this solution since it still involves an integral over the gravitational potentials, I urge you to reconsider. First, look at Figure 8.6, which compares the solution of Eq. (8.24) with exact results obtained by integrating the full set of coupled Einstein–Boltzmann equations. The approximate solution gets the peak locations dead on, and it does fairly well with the heights as well. The later peaks — those at $k\eta_0 > 500$ — are

---

[5]You can rectify this by applying the WKB approximation in Exercise 5.
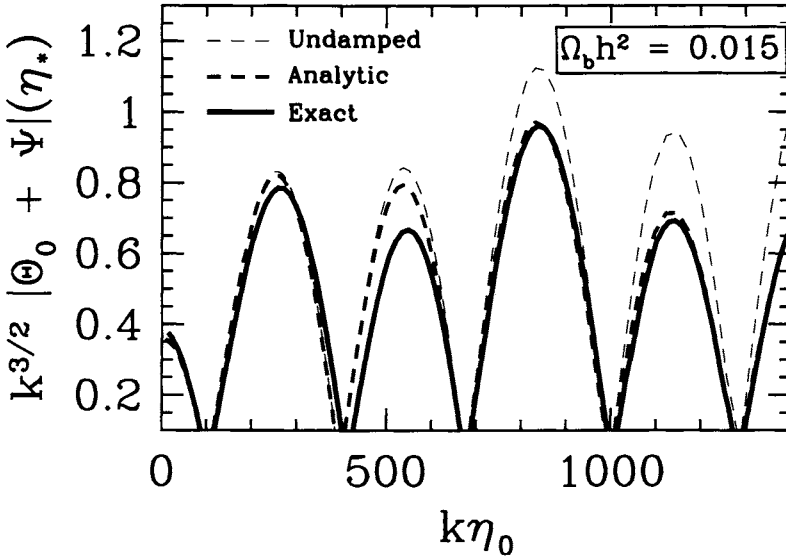
Figure 8.6. The monopole at recombination in a standard CDM model. The exact solution is the heavily weighted solid line. The light dashed line is the undamped solution of Section 8.3, Eq. (8.24); the heavier curve in the middle accounts for damping using the treatment of Section 8.4.

clearly overestimated by our solution, but we will shortly rectify this when we include damping due to diffusion in the next section. A second reason to respect the approximate solution is that it divides the problem neatly into first (i) a calculation of the external gravitional potentials generated by the dark matter and then (ii) the effect of these potentials on the anisotropies. Third, the solution clearly illustrates that the cosine mode is the one excited by inflationary models. This is important, because it is very hard to imagine this mode excited by any other mechanism. If causality is respected, then there should be no perturbations with $k\eta \ll 1$ early on. We know that inflation evades this constraint by changing the true horizon; it is tempting to say that if this mode is observed, we are seeing evidence for inflation. Fourth, we now have a more accurate expression for the frequency of oscillations and therefore for the locations of the acoustic peaks. In the limit that the first term in Eq. (8.24) dominates, the peaks should appear at the extrema of $\cos(kr_s)$, e.g., at

$$k_{\mathrm{p}} = n\pi/r_s \qquad n = 1, 2, \ldots \qquad . \qquad (8.25)$$

And the final reason Eq. (8.24) is impressive is that the full set of Einstein–Boltzmann equations involve literally thousands of coupled variables (e.g., the Θ_l's). Reducing those thousands of differential equations to just one is a huge leap in knowledge.

In addition to the monopole, the photon distribution has a nonnegligible dipole at recombination. Using Eq. (8.12), we can obtain an analytic solution for the dipole by differentiating Eq. (8.24):

$$\Theta_1(\eta) = \frac{1}{\sqrt{3}} \left[\Theta_0(0) + \Phi(0) \right] \sin(kr_s)$$

$$- \frac{k}{3} \int_0^\eta d\eta' \left[\Phi(\eta') - \Psi(\eta') \right] \cos \left[k(r_s(\eta) - r_s(\eta')) \right]. \tag{8.26}$$

The first term is completely out of phase with the monopole ($\sin(kr_s)$ versus $\cos(kr_s)$). Figure 8.7 shows that this feature remains even after accounting for the integral term. This mismatch of phase will have important implications for the final anisotropy spectrum.
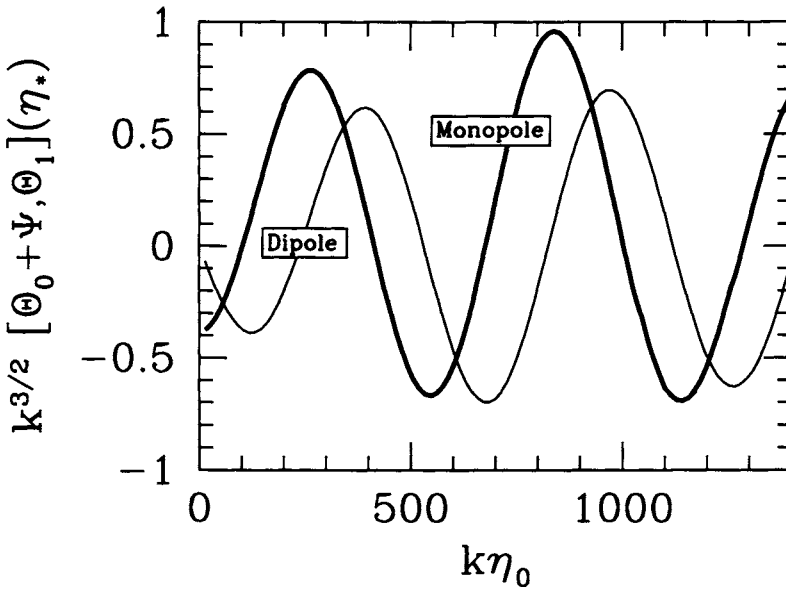
Figure 8.7. The monopole and dipole at recombination in a standard CDM model. The dipole vanishes for the longest wavelength modes that have not entered the horizon by recombination. It is completely out of phase with the monopole.

8.4 DIFFUSION DAMPING

Figure 8.6 makes it clear that we must account for diffusion to get accurate CMB spectra. To analyze diffusion quantitatively, we must return to the equations for the moments of the photon distribution, Eqs. (8.12), (8.13) and (8.10). Until now, we have neglected Θ_2 and all higher moments. Diffusion is characterized by a small but nonnegligible quadrupole.

We must therefore supplement the set of equations we wrote down in the last section with an equation for the quadrupole, Θ_2. Our task is somewhat simplified by the fact that we will be interested in phenomena occurring only on small scales. On these scales, recall from Chapter 7 (e.g., Figure 7.8) that the potentials are very small because of radiation pressure, so we can drop Φ and Ψ everywhere. Also, we will see that diffusion manifests itself in the moments by making each successive moment proportional to a higher power of $1/\dot{\tau}$. Thus we will need to keep only the $l = 2$ mode; all higher ones can be neglected. With these approximations, we have

$$\dot{\Theta}_0 + k\Theta_1 = 0 \qquad (8.27)$$

$$\dot{\Theta}_1 + k\left(\frac{2}{3}\Theta_2 - \frac{1}{3}\Theta_0\right) = \dot{\tau}\left(\Theta_1 - \frac{iv_b}{3}\right) \qquad (8.28)$$

$$\dot{\Theta}_2 - \frac{2k}{5}\Theta_1 = \frac{9}{10}\dot{\tau}\Theta_2. \qquad (8.29)$$

These three equations need to be supplemented by an equation for v_b. This is best expressed as a slight rewriting of Eq. (8.14):

$$3i\Theta_1 + v_b = \frac{R}{\dot{\tau}}\left[\dot{v}_b + \frac{\dot{a}}{a}v_b\right], \qquad (8.30)$$

where again I have dropped the gravitational potential.

To solve this set of equations, we appeal to the high-frequency nature of damping. Let us write the time dependence of the velocity as

$$v_b \propto e^{i\int \omega d\eta} \qquad (8.31)$$

and similarly for all other variables. We already know that $\omega \simeq kc_s$ in the tightly coupled limit. Now we are searching for damping, an imaginary part to ω. Since damping occurs on small scales, or high frequencies,

$$\dot{v}_b = i\omega v_b \gg \frac{\dot{a}}{a}v_b; \qquad (8.32)$$

$\dot{a}/a$ is of order η^{-1} while ω is of order k. So we can drop the second term on the right in Eq. (8.30) and the velocity equation then becomes

$$v_b = -3i\Theta_1\left[1 - \frac{i\omega R}{\dot{\tau}}\right]^{-1}$$

$$\simeq -3i\Theta_1\left[1 + \frac{i\omega R}{\dot{\tau}} - \left(\frac{\omega R}{\dot{\tau}}\right)^2\right] \qquad (8.33)$$

where I have expanded out to $\dot{\tau}^{-2}$ because $v_b + 3i\Theta_1$ is multiplied by $\dot{\tau}$ in Eq. (8.28).

The equation for the second moment of the photon field, (8.29), can be reduced similarly. First we can drop the $\dot{\Theta}_2$ term since it is much smaller than $\dot{\tau}\Theta_2$. This leaves simply

$$\Theta_2 = -\frac{4k}{9\dot{\tau}}\Theta_1 \tag{8.34}$$

which shows that our approximation scheme is controlled: higher moments are suppressed by additional powers of $k/\dot{\tau}$. The equation for the zeroth moment becomes

$$i\omega\Theta_0 = -k\Theta_1. \tag{8.35}$$

Inserting all of these into Eq. (8.28) gives the dispersion relation

$$i\omega - \frac{8k^2}{27\dot{\tau}} + (k^2/3i\omega) = \dot{\tau}\left(1 - \left[1 + \frac{i\omega R}{\dot{\tau}} - \left(\frac{\omega R}{\dot{\tau}}\right)^2\right]\right). \tag{8.36}$$

Collecting terms we get

$$\omega^2(1+R) - \frac{k^2}{3} + \frac{i\omega}{\dot{\tau}}\left[\omega^2 R^2 + \frac{8k^2}{27}\right] = 0. \tag{8.37}$$

The first two terms on the left, the leading ones in the expansion of $1/\dot{\tau}$, recover the result of the previous section, that the frequency is the wavenumber times the speed of sound. We can write the frequency as this zero-order piece plus a first-order correction, $\delta\omega$. Then, inserting the zero-order part into the terms inversely proportional to $\dot{\tau}$ leads to

$$\delta\omega = -\frac{ik^2}{2(1+R)\dot{\tau}}\left[c_s^2 R^2 + \frac{8}{27}\right]. \tag{8.38}$$

Therefore, the time dependence of the perturbations is

$$\Theta_0, \Theta_1 \sim \exp\left\{ik\int d\eta c_s\right\}\exp\left\{-\frac{k^2}{k_D^2}\right\} \tag{8.39}$$

where the damping wavenumber is defined via

$$\frac{1}{k_D^2(\eta)} \equiv \int_0^\eta \frac{d\eta'}{6(1+R)n_e\sigma_T a(\eta')}\left[\frac{R^2}{(1+R)} + \frac{8}{9}\right]. \tag{8.40}$$

Putting aside factors of order unity, this equation says that $1/k_D \sim [\eta/n_e\sigma_T a]^{1/2}$, which agrees with our heuristic estimate at the beginning of this chapter.

As a first estimate of the damping scale, we can work in the prerecombination limit, in which all electrons (except those in helium) are free. In Chapter 3 we estimated the optical depth in this limit, but ignored helium. The mass fraction of helium is usually denoted as Y_p and is approximately 0.24. Since each helium nucleus contains four nucleons, the ratio of helium to the total number of nuclei is $Y_p/4$. Each of these absorbs two electrons (one for each proton), so when counting

the number of free electrons before hydrogen recombination, we must multiply our estimate of Eq. (3.46) by $1 - Y_p/2$. Using the fact that $H_0 = 3.33 \times 10^{-4}\,h\,\mathrm{Mpc}^{-1}$, we have, in the prerecombination limit,

$$n_e \sigma_T a = 2.3 \times 10^{-5} \mathrm{Mpc}^{-1} \Omega_b h^2 a^{-2} \left(1 - \frac{Y_p}{2}\right). \qquad (8.41)$$

Using this, you can show (Exercise 8) that an approximation for the damping scale is

$$k_D^{-2} = 3.1 \times 10^6\,\mathrm{Mpc}^2 a^{5/2} f_D(a/a_{\mathrm{eq}}) \left(\Omega_b h^2\right)^{-1} \left(1 - \frac{Y_p}{2}\right)^{-1} \left(\Omega_m h^2\right)^{-1/2} \quad (8.42)$$

where f_D, defined in Eq. (8.88), goes to 1 as a/a_{eq} gets large.
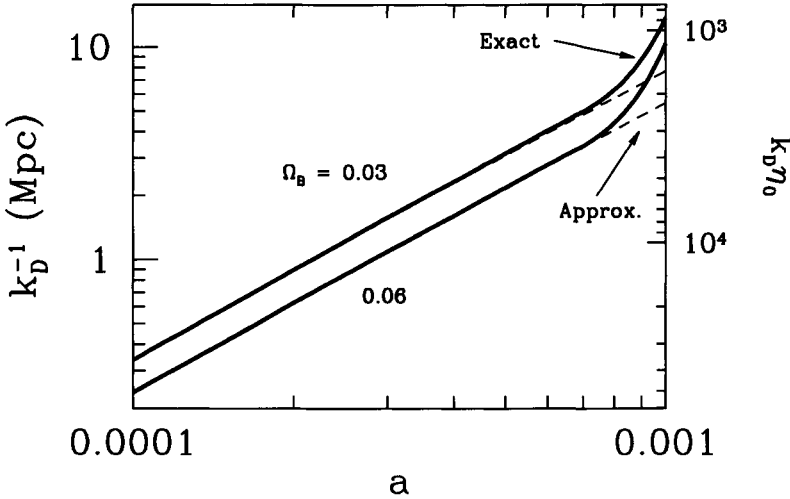
Figure 8.8. Damping scale as a function of the scale factor for two different values of Ω_b (with $h = 0.5$). Heavy curves (exact) numerically integrate over the standard recombination history, while light curves use the approximation of Eq. (8.42) which assumes electrons remain ionized. Right axis shows the equivalent $k_D \eta_0$; damping occurs on angular scales $l > k_D \eta_0$.

Figure 8.8 shows the evolution of the damping scale before recombination. Neglecting recombination is a good approximation at early times but, as expected, leads to quantitative errors right near η_*, when using Eq. (8.41) for the free electron density does not accurately account for the electrons swept up into neutral hydrogen. In the absence of recombination, k_D scales as $\Omega_b^{1/2}$. Note from the late time behavior in Figure 8.8 that the messy details of recombination change this simple scaling: k_D for the $\Omega_b = 0.06$ case is less than $2^{0.5}$ as big as the $\Omega_b = 0.03$ case.

Figure 8.8 requires one final comment. The damping of anisotropies due to photon diffusion is sometimes referred to as being caused by the "finite thickness of

the last scattering surface." That is, it is argued that if recombination took place instantaneously at η_*, then there would be no damping. Figure 8.8 shows that this is patently false. Even if recombination had occurred in this way, the universe before recombination would *not* have been inifinitely optically thick. Photons would still stream a reasonable distance and hence damp anisotropies. In the examples shown, the damping scale would have been smaller (larger l) by less than a factor of 2 if recombination had occurred instantaneously. On the other hand, we will see in the next section that the anisotropies today are determined by integrating over the *visibility function*, essentially a filter centered at the epoch of recombination but broadened due to the finite thickness of the last scattering surface. When incorporating the effects of damping (Seljak, 1994; Hu and Sugiyama, 1995), one must account for this finite thickness by integrating the damping function e^{-k^2/k_D^2} weighted by the visibility function. Thus the finite thickness of the last scattering surface has both qualitative and quantitative effects on the final anisotropy spectrum.

8.5 INHOMOGENEITIES TO ANISOTROPIES

We now have a good handle on the perturbations to the photons at recombination. It is time to transform this understanding into predictions for the anisotropy spectrum today. First, we will solve for the moments Θ_l today in the next subsection. Then we will spend a bit of time relating these moments to the observables. Thus the main purpose of the following subsections is to derive Eq. (8.56), which relates the moments today to the monopole and dipole at recombination, and Eq. (8.68), which expresses the CMB power spectrum in terms of the Fourier moments today.

8.5.1 Free Streaming

We want to derive a formal solution for the photon moments today $\Theta_l(\eta_0)$ in terms of the monopole and dipole at recombination. A formal solution can be obtained by returning to Eq. (4.100). Subtracting $\dot{\tau}\Theta$ from both sides leads to

$$\dot{\Theta} + (ik\mu - \dot{\tau})\Theta = e^{-ik\mu\eta + \tau}\frac{d}{d\eta}\left[\Theta e^{ik\mu\eta - \tau}\right] = \tilde{S} \qquad (8.43)$$

where the source function is defined as

$$\tilde{S} \equiv -\dot{\Phi} - ik\mu\Psi - \dot{\tau}\left[\Theta_0 + \mu v_b - \frac{1}{2}\mathcal{P}_2(\mu)\Pi\right]. \qquad (8.44)$$

Hold your curiosity about the $\tilde{}$ in the definition. Multplying both sides of Eq. (8.43) by the exponential and then integrating over η leads directly to

$$\Theta(\eta_0) = \Theta(\eta_{\text{init}})e^{ik\mu(\eta_{\text{init}} - \eta_0)}e^{-\tau(\eta_{\text{init}})} + \int_{\eta_{\text{init}}}^{\eta_0} d\eta \tilde{S}(\eta)e^{ik\mu(\eta - \eta_0) - \tau(\eta)} \qquad (8.45)$$

where I have used the fact that $\tau(\eta = \eta_0) = 0$ since τ is defined as the scattering rate integrated from η up to η_0. We also know that, if the initial time η_{init} is early

enough, then the optical depth $\tau(\eta_{\text{init}})$ will be extremely large. Therefore, the first term on the right side of Eq. (8.45) vanishes. This corresponds to the fact that any initial anisotropy is completely erased by Compton scattering. By the same reasoning, we can set the lower limit on the integral to zero: any contribution to the integrand from $\eta < \eta_{\text{init}}$ is completely negligible. Thus, the solution for the perturbations is

$$\Theta(k, \mu, \eta_0) = \int_0^{\eta_0} d\eta \tilde{S}(k, \mu, \eta) e^{ik\mu(\eta - \eta_0) - \tau(\eta)}. \qquad (8.46)$$

Equation (8.46) looks simple, but of course all of the complication is hidden in the source function $\tilde{S}$. Notice that $\tilde{S}$ depends somewhat on the angle μ. If it did *not* depend on μ, we could immediately turn Eq. (8.46) into an equation for each of the Θ_l's. For, we could multiply each side by the Legendre polynomial $\mathcal{P}_l(\mu)$ and then integrate over all μ. By Eq. (4.99), the left side would give $(-i)^l \Theta_l$ and the right would contain the integral

$$\int_{-1}^{1} \frac{d\mu}{2} \mathcal{P}_l(\mu) e^{ik\mu(\eta - \eta_0)} = \frac{1}{(-i)^l} j_l \left[k(\eta - \eta_0) \right] \qquad (8.47)$$

where j_l is the spherical Bessel function. This approach looks so promising that we should pursue it to its end, again forgetting for the moment that $\tilde{S}$ really does have some μ dependence. The expression for Θ_l would be

$$\Theta_l(k, \eta_0) = (-1)^l \int_0^{\eta_0} d\eta \tilde{S}(k, \eta) e^{-\tau(\eta)} j_l \left[k(\eta - \eta_0) \right]. \qquad (8.48)$$

What about the μ dependence in $\tilde{S}$? We can account for this by noting that $\tilde{S}$ multiplies the exponential $e^{ik\mu(\eta - \eta_0)}$ in Eq. (8.46). Thus, everywhere we encounter a factor of μ in $\tilde{S}$ we can replace it with a time derivative:

$$\mu \rightarrow \frac{1}{ik} \frac{d}{d\eta}. \qquad (8.49)$$

Let me demonstrate this explicitly with the $-ik\mu\Psi$ term in $\tilde{S}$. The integral is

$$-ik \int_0^{\eta_0} d\eta \, \mu \Psi e^{ik\mu(\eta - \eta_0) - \tau(\eta)} = -\int_0^{\eta_0} d\eta \Psi e^{-\tau(\eta)} \frac{d}{d\eta} e^{ik\mu(\eta - \eta_0)}$$

$$= \int_0^{\eta_0} d\eta e^{ik\mu(\eta - \eta_0)} \frac{d}{d\eta} \left[\Psi e^{-\tau(\eta)} \right] \qquad (8.50)$$

where the last line follows by integration by parts. Note that the surface terms can be dropped: at $\eta = 0$ they are damped by the $e^{-\tau(0)}$ factor. The terms at $\eta = \eta_0$ are not small, but they are irrelevant since they have no angular dependence. They alter the monopole, an alteration which we cannot detect. Thus, accounting for the integration by parts changes the substitution rule of Eq. (8.49) by a minus sign,

with the understanding that the derivative does *not* act on the oscillating part of the exponential, $e^{ik\mu(\eta-\eta_0)}$. The solution in Eq. (8.48) therefore becomes

$$\Theta_l(k,\eta_0) = \int_0^{\eta_0} d\eta S(k,\eta) j_l\left[k(\eta_0-\eta)\right] \tag{8.51}$$

with the source function now defined as

$$S(k,\eta) \equiv e^{-\tau}\left[-\dot{\Phi}-\dot{\tau}\left(\Theta_0+\frac{1}{4}\Pi\right)\right]$$

$$+\frac{d}{d\eta}\left[e^{-\tau}\left(\Psi-\frac{iv_b\dot{\tau}}{k}\right)\right] - \frac{3}{4k^2}\frac{d^2}{d\eta^2}\left[e^{-\tau}\dot{\tau}\Pi\right]. \tag{8.52}$$

In Eq. (8.51), I have also used the property of spherical Bessel functions: $j_l(x) = (-1)^l j_l(-x)$.

At this stage, it is useful to introduce the *visibility function*
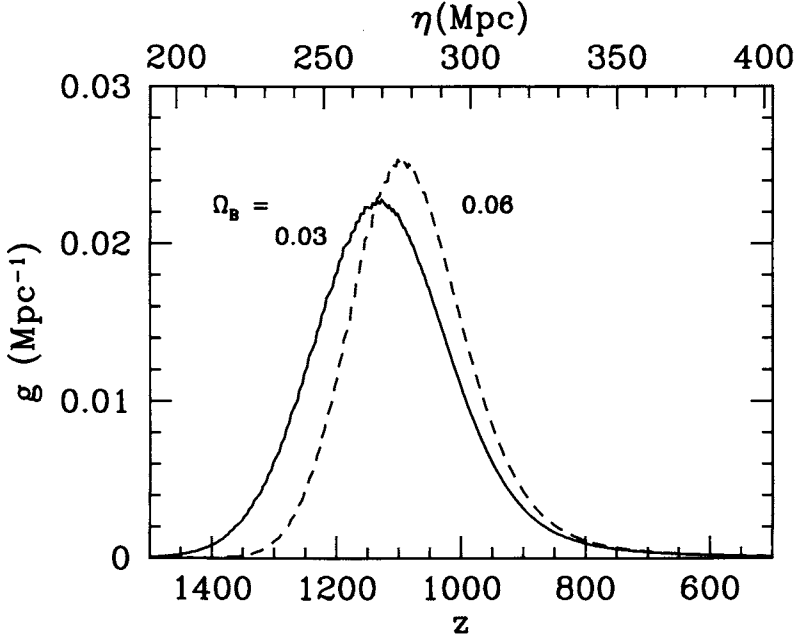
$$g(\eta) \equiv -\dot{\tau}e^{-\tau}. \tag{8.53}$$

The visibility function has some interesting properties. The integral $\int_0^{\eta_0} d\eta g(\eta) = 1$, so we can think of it as a probability density. It is the probability that a photon last scattered at η. In the standard recombination, since τ is so large early on, this probability is essentially zero for η earlier than the time of recombination. It also declines rapidly after recombination, because the prefactor $-\dot{\tau}$, which is the scattering rate, is quite small. Figure 8.9 shows the visibility function for two values of the baryon density.

The source function in Eq. (8.52) can now be expressed in terms of the visibility function. If we drop the polarization tensor Π in the source since it is very small, then the source function becomes

$$S(k,\eta) \simeq g(\eta)\left[\Theta_0(k,\eta)+\Psi(k,\eta)\right]$$

$$+\frac{d}{d\eta}\left(\frac{iv_b(k,\eta)g(\eta)}{k}\right)$$

$$+e^{-\tau}\left[\dot{\Psi}(k,\eta)-\dot{\Phi}(k,\eta)\right]. \tag{8.54}$$

We can take our analytic solution one step further by performing the time integral in Eq. (8.51). The source term proportional to v_b is best treated by integrating by parts. Then,

$$\Theta_l(k,\eta_0) = \int_0^{\eta_0} d\eta\, g(\eta)\,\left[\Theta_0(k,\eta)+\Psi(k,\eta)\right]\, j_l\left[k(\eta_0-\eta)\right]$$

$$-\int_0^{\eta_0} d\eta\, g(\eta)\,\frac{iv_b(k,\eta)}{k}\,\frac{d}{d\eta}j_l\left[k(\eta_0-\eta)\right]$$

Figure 8.9. The visibility function. Most electrons last scatter at around $z \simeq 1100$ with little dependence on the baryon density. Note that the integral of g over conformal time is 1. Here $h = 0.5$.

$$+ \int_0^{\eta_0} d\eta \; e^{-\tau} \left[\dot{\Psi}(k, \eta) - \dot{\Phi}(k, \eta) \right] \; j_l \left[k(\eta_0 - \eta) \right]. \qquad (8.55)$$

There are two types of terms in Eq. (8.55). First, there are those wherein the integral is weighted by $e^{-\tau}$. These contribute as long as $\tau \lesssim 1$, that is, at all times after recombination. Note that these are also proportional to derivatives of the potentials. If the potentials are constant after recombination, these terms vanish. In many theories, as we saw in Chapter 7, this is precisely what happens: the universe is purely matter dominated after recombination and in such an environment, the potentials generally remain constant. The corrections due to changing potentials are therefore important to get things right quantitatively, but do not affect the qualitative structure of the anisotropy spectrum. Rather, the dominant terms in Eq. (8.55) are the second types of terms, the ones with integrals weighted by the visibility function.

Since the visibility function is so sharply peaked, the integrals in the first two terms become very simple. To see why, consider Figure 8.10 which shows the three parts of the integrand of the first term (the monopole) in Eq. (8.55). Since the visibility function changes rapidly compared with the other two functions, we can evaluate those other functions at the peak of the visibility function, i.e., at $\eta = \eta_*$, and remove them from the integral. But then, the integral is simply $\int d\eta g(\eta) = 1$. Thus, we are left with

$$\eta(\text{Mpc})$$
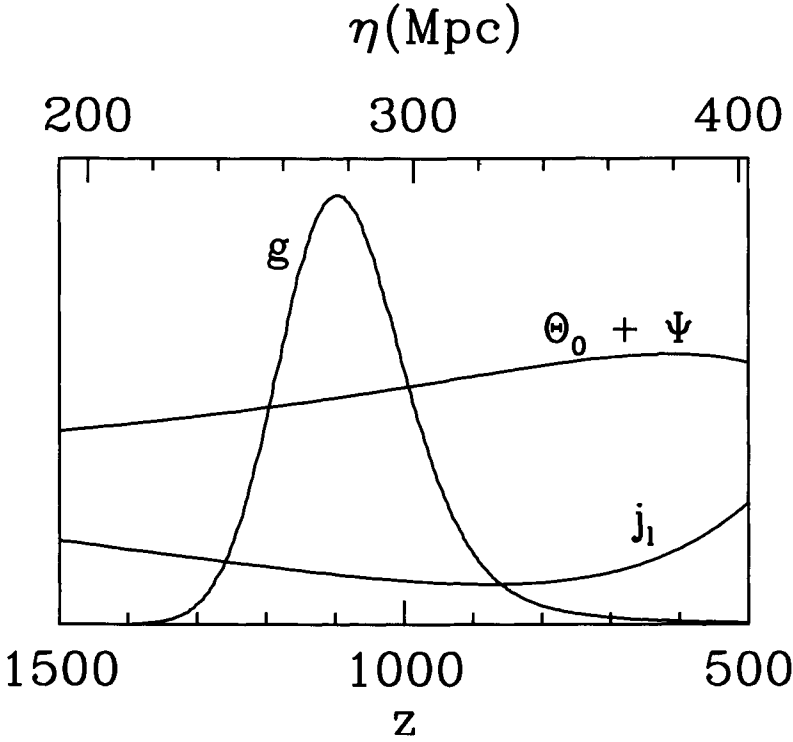
Figure 8.10. The three components of the integrand in the monopole term of Eq. (8.55). The visibility function is sharply peaked, so it changes rapidly compared with the monopole $\Theta_0 + \Psi$ and the Bessel function $j_l(k[\eta - \eta_0])$. Figure is for $l = 100, k = 0.013\,h\,\text{Mpc}^{-1}$.

$$\Theta_l(k,\eta_0) \simeq [\Theta_0(k,\eta_*) + \Psi(k,\eta_*)]\; j_l\,[k(\eta_0 - \eta_*)]$$

$$+ 3\Theta_1(k,\eta_*)\left(j_{l-1}\,[k(\eta_0 - \eta_*)] - \frac{(l+1)j_l\,[k(\eta_0 - \eta_*)]}{k(\eta_0 - \eta_*)}\right)$$

$$+ \int_0^{\eta_0} d\eta\; e^{-\tau}\left[\dot{\Psi}(k,\eta) - \dot{\Phi}(k,\eta)\right]\; j_l\,[k(\eta_0 - \eta)]. \tag{8.56}$$

Here I have used the spherical Bessel function identity of Eq. (C.18) to rewrite the Bessel function derivative in the velocity term and also the fact that $v_b \simeq -3i\Theta_1$ at η_*. On scales much smaller than the one shown in Figure 8.10, $\Theta_0 + \Psi$ changes more rapidly because of the rapid change in the damping scale around recombination. However, this effect can be incorporated by modifying the damping function from

$$e^{-k^2/k_D(\eta_*)^2} \rightarrow \int d\eta g(\eta)e^{-k^2/k_D(\eta)^2}. \tag{8.57}$$

Equation (8.56) is the basis for semianalytic calculations (Seljak, 1994; Hu and Sugiyama, 1995) of C_l spectra which agree with the exact (numerical) solutions to

within 10%. From Eq. (8.56), we see that, to solve for the anisotropies today, we must know the monopole (Θ_0), dipole (Θ_1), and potential (Ψ) at the time of recombination. Further, there will be small but noticable corrections if the potentials are time dependent. These corrections, encoded in the last line of Eq. (8.56), are often called *integrated Sachs–Wolfe* (ISW) terms.

The monopole term — the first in Eq. (8.56) — is precisely what we expected from the rough arguments of Section 8.1. In particular, the spherical Bessel function, $j_l[k(\eta_0 - \eta_*)]$, determines how much anisotropy on an angular scale l^{-1} is contributed by a plane wave with wavenumber k. On very small angular scales,

$$\lim_{l \to \infty} j_l(x) = \frac{1}{l} \left(\frac{x}{l} \right)^{l-1/2} . \tag{8.58}$$

That is, $j_l(x)$ is extremely small for large l when $x < l$. In our case, this means that $\Theta_l(k, \eta_0)$ is very close to zero for $l > k\eta_0$. This makes sense physically. Returning to Figure 8.4, we see that very small angular scales will see little anisotropy from a perturbation with a large wavelength. The converse is also true: angular scales larger than $1/(k\eta_0)$ get little contribution from such a perturbation. To sum up, a perturbation with wavenumber k contributes predominantly on angular scales of order $l \sim k\eta_0$. One last comment about the monopole term: the final anisotropy today depends on not just Θ_0, but rather $\Theta_0 + \Psi$, again something we anticipated since photons must climb out of their potential wells to reach us today.

8.5.2 The C_l's

How is the observed anisotropy pattern today related to the rather abstract $\Theta_l(k, \eta_0)$? To answer this question, we must first describe the way in which the temperature field is characterized today and then relate this characterization to Θ_l.

Recall that in Eq. (4.34), we wrote the temperature field in the universe as

$$T(\vec{x}, \hat{p}, \eta) = T(\eta) \left[1 + \Theta(\vec{x}, \hat{p}, \eta) \right] . \tag{8.59}$$

Although this field is defined at every point in space and time, we can observe it only here (at $\vec{x}_0$) and now (at η_0).[6] Our only handle on the anisotropies is their dependence on the direction of the incoming photons, $\hat{p}$. So all the richness we observe comes from the changes in the temperature as the direction vector $\hat{p}$ changes. Observers typically makes maps, wherein the temperature is reported at a number of incoming directions, or "spots on the sky." These spots are labeled not by the $\hat{p}_x, \hat{p}_y, \hat{p}_z$ components of $\hat{p}$, but rather by polar coordinates θ, ϕ. However, it

---

[6]We do make small excursions from this point in space-time. For example, satellites are not located on Earth and anisotropy measurements have been made over the past 30 years. These are completely insignificant on scales over which the temperature is varying, which are of order the Hubble time (or distance).

is a simple matter to move back and forth between the 3D unit vector $\hat{p}$ and polar coordinates.[7] I'll stick with $\hat{p}$ in the ensuing derivation.

We now expand the field in terms of spherical harmonics. That is, we write

$$\Theta(\vec{x}, \hat{p}, \eta) = \sum_{l=1}^{\infty} \sum_{m=-l}^{l} a_{lm}(\vec{x}, \eta) Y_{lm}(\hat{p}). \qquad (8.60)$$

The subscripts l, m are conjugate to the real space unit vector $\hat{p}$, just as the variable $\vec{k}$ is conjugate to the Fourier transform variable $\vec{x}$. We are all familiar with Fourier transforms, so it is useful to think of the expansion in terms of spherical harmonics as a kind of generalized Fourier transform. Whereas the complete set of eigenfunctions for the Fourier transform are $e^{i\vec{k}\cdot\vec{x}}$, here the complete set of eigenfunctions for expansion on the surface of a sphere are $Y_{lm}(\hat{p})$. All of the information contained in the temperature field T is also contained in the space-time dependent amplitudes a_{lm}. As an example of this, consider an experiment which maps the full sky with an angular resolution of 7°. The full sky has 4π radians$^2 \simeq 41,000$ degrees^2, so there are 840 pixels with area of $(7°)^2$. Thus, such an experiment would have 840 independent pieces of information. Were we to characterize this information with a_{lm}'s instead of temperatures in pixels, there would be some $l_{\max}$ above which there is no information. One way to determine this $l_{\max}$ is to set the total number of recoverable a_{lm}'s as $\sum_{l=0}^{l_{\max}}(2l+1) = (l_{\max}+1)^2 = 840$. So the information could be equally well characterized by specifying all the a_{lm}'s up to $l_{\max} = 28$. Incidentally, this is a fairly good caricature of the COBE experiment (Smoot et al., 1992; Bennett et al., 1996). They presented temperature data over many more pixels, but many of these pixels were overlapping. So, the independent information was contained in multipoles up to $l \sim 30$. Experiments currently under way or well along in the planning stage are capable of measuring the moments all the way up to $l \sim 10^4$.

We want to relate the observables, the a_{lm}'s, to the Θ_l we have been dealing with. To do this, we can use the orthogonality property of the spherical harmonics. The Y_{lm}'s are normalized via Eq. (C.11),

$$\int d\Omega Y_{lm}(\hat{p}) Y_{l'm'}^*(\hat{p}) = \delta_{ll'}\delta_{mm'}, \qquad (8.61)$$

where Ω is the solid angle spanned by $\hat{p}$. Therefore the expansion of Θ in terms of spherical harmonics, Eq. (8.60), can be inverted by multiplying both sides by $Y_{lm}^*(\hat{p})$ and integrating:

$$a_{lm}(\vec{x}, \eta) = \int \frac{d^3k}{(2\pi)^3} e^{i\vec{k}\cdot\vec{x}} \int d\Omega Y_{lm}^*(\hat{p}) \Theta(\vec{k}, \hat{p}, \eta). \qquad (8.62)$$

Here I have written the right-hand side in terms of the Fourier transform $(\Theta(\vec{k})$ instead of $\Theta(\vec{x}))$, since that is the quantity for which we obtained solutions.

---

[7]$\hat{p}_z = \cos\theta$, $\hat{p}_x = \sin\theta\cos\phi$, and $\hat{p}_y = \sin\theta\sin\phi$.
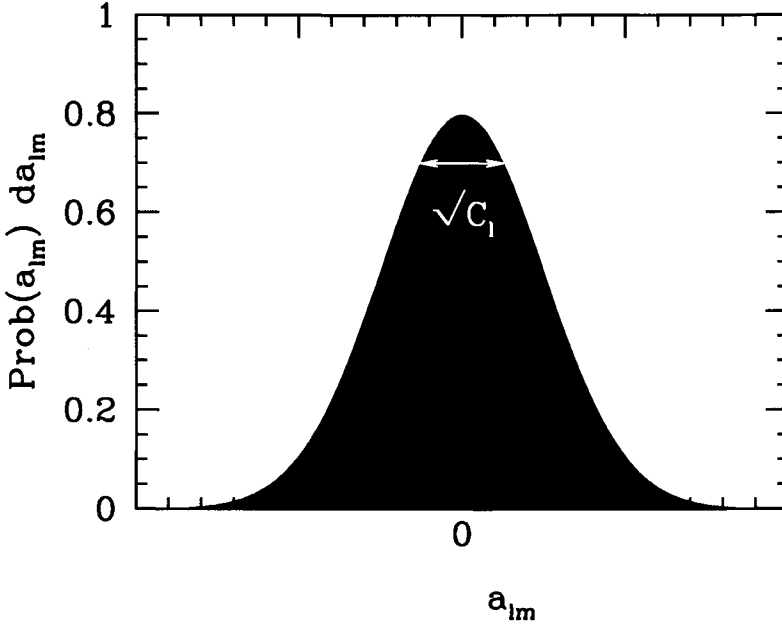
Figure 8.11. The distribution from which the a_{lm}'s are drawn. The distribution has expectation equal to zero and a width of $C_l^{1/2}$.

As with the density perturbations, we cannot make predictions about any particular a_{lm}, just about the distribution from which they are drawn, a distribution which traces its origin to the quantum fluctuations first laid down during inflation. Figure 8.11 illustrates this distribution. The mean value of all the a_{lm}'s is zero, but they will have some nonzero variance. The variance of the a_{lm}'s is called C_l. Thus,

$$\langle a_{lm} \rangle = 0 \qquad ; \qquad \langle a_{lm} a^*_{l'm'} \rangle = \delta_{ll'} \delta_{mm'} C_l. \qquad (8.63)$$

It is very important to note that, for a given l, each a_{lm} has the same variance. For $l = 100$, say, all 201 $a_{100,m}$'s are drawn from the same distribution. When we measure these 201 coefficients, we are sampling the distribution. This much information will give us a good handle on the underlying variance of the distribution. On the other hand, if we measure the five components of the quadrupole ($l = 2$), we do not get very much information about the underlying variance, C_2. Thus, *there is a fundamental uncertainty in the knowledge we may get about the C_l's.* This uncertainty, which is most pronounced at low l, is called *cosmic variance.* Quantitatively, the uncertainty scales simply as the inverse of the square root of the number of possible samples, or

$$\left(\frac{\Delta C_l}{C_l} \right)_{\text{cosmic variance}} = \sqrt{\frac{2}{2l+1}}. \qquad (8.64)$$

We can now obtain an expression for C_l in terms of $\Theta_l(k)$. First we square a_{lm} in Eq. (8.62) and take the expectation value of the distribution. For this we need $\langle \Theta(\vec{k}, \hat{p}) \Theta^*(\vec{k}', \hat{p}') \rangle$, where from now on we will keep the η dependence implicit. This expectation value is complicated because it depends on two separate phenomena: (i) the initial amplitude and phase of the perturbation is chosen during inflation from a Gaussian distribution and (ii) the evolution we have studied in this chapter turns this initial perturbation into anisotropies, i.e. produces the dependence on $\hat{p}$. To simplify then, it makes sense to separate these two phenomena and write the photon distribution as $\delta \times (\Theta/\delta)$, where the dark matter overdensity δ does not depend on any direction vector. The ratio Θ/δ is precisely what we have solved for in the last two chapters: given the initial amplitude of a mode, we have learned how to evolve forward in time. The ratio does *not* depend on the initial amplitude, so it can be removed from the averaging over the distribution. Therefore,

$$\langle \Theta(\vec{k}, \hat{p}) \Theta(\vec{k}', \hat{p}') \rangle = \langle \delta(\vec{k}) \delta^*(\vec{k}') \rangle \frac{\Theta(\vec{k}, \hat{p})}{\delta(\vec{k})} \frac{\Theta^*(\vec{k}', \hat{p})}{\delta^*(\vec{k}')}$$

$$= (2\pi)^3 \delta^3(\vec{k} - \vec{k}') P(k) \frac{\Theta(k, \hat{k} \cdot \hat{p})}{\delta(k)} \frac{\Theta^*(k, \hat{k} \cdot \hat{p}')}{\delta^*(k)}, \quad (8.65)$$

where the second equality uses the definition of the matter power spectrum $P(k)$, but also contains a subtlety in the ratio Θ/δ. This ratio, which is determined solely by the evolution of both δ and Θ, depends only on the magnitude of $\vec{k}$ and the dot product $\hat{k} \cdot \hat{p}$. Two modes with the same k and $\hat{k} \cdot \hat{p}$ evolve identically even though their initial amplitudes and phases are different.

After squaring Eq. (8.62), we see that the anisotropy spectrum is

$$C_l = \int \frac{d^3k}{(2\pi)^3} P(k) \int d\Omega Y_{lm}^*(\hat{p}) \frac{\Theta(k, \hat{k} \cdot \hat{p})}{\delta(k)} \int d\Omega' Y_{lm}(\hat{p}') \frac{\Theta^*(k, \hat{k} \cdot \hat{p}')}{\delta^*(k)}. \quad (8.66)$$

Now we can expand $\Theta(k, \hat{k} \cdot \hat{p}')$ and $\Theta(k, \hat{k} \cdot \hat{p}')$ in spherical harmonics using the inverse of Eq. (4.99), $\Theta(k, \hat{k} \cdot \hat{p}) = \sum_l (-i)^l (2l + 1) \mathcal{P}_l(\hat{k} \cdot \hat{p}) \Theta_l(k)$. This leaves

$$C_l = \int \frac{d^3k}{(2\pi)^3} P(k) \sum_{l'l''} (-i)^{l'} (i)^{l''} (2l' + 1)(2l'' + 1) \frac{\Theta_{l'}(k) \Theta_{l''}^*(k)}{|\delta(k)|^2}$$

$$\times \int d\Omega \mathcal{P}_{l'}(\hat{k} \cdot \hat{p}) Y_{lm}^*(\hat{p}) \int d\Omega' \mathcal{P}_{l''}(\hat{k} \cdot \hat{p}') Y_{lm}(\hat{p}'). \quad (8.67)$$

The two angular integrals here (Exercise 9) are identical. They are nonzero only if $l' = l$ and $l'' = l$, in which case they are equal to $4\pi Y_{lm}(\hat{k})/(2l + 1)$ (or the complex conjugate). The angular part of the d^3k integral then becomes an integral over $|Y_{lm}|^2$, which is just equal to 1, leaving

$$C_l = \frac{2}{\pi} \int_0^\infty dk \, k^2 \, P(k) \left| \frac{\Theta_l(k)}{\delta(k)} \right|^2. \quad (8.68)$$

For a given l, then, the variance of a_{lm}, C_l, is an integral over all Fourier modes of the variance of $\Theta_l(\vec{k})$. We can now use Eqs. (8.56) and (8.68) to plot the anisotropy spectrum today.

8.6 THE ANISOTROPY SPECTRUM TODAY

8.6.1 Sachs–Wolfe Effect

Large-angle anisotropies are not affected by any microphysics: at the time of recombination, the perturbations responsible for these anisotropies were on scales far larger than could be connected via causal processes. On these largest of scales, only the monopole contributes to the anisotropy; this is the first term in Eq. (8.56). So the large-angle anisotropy is determined by $\Theta_0 + \Psi$ evaluated at recombination. The large-scale solution we found in Eq. (8.6) was that this combination is equal to $\Psi(\eta_*)/3$. In most cosmological models, recombination occurs far enough after matter/radiation equality that we can approximate the potential back then to be equal to the potential today modulo the growth factor, so

$$\Theta_0(\eta_*) + \Psi(\eta_*) \simeq \frac{1}{3D_1(a=1)}\Psi(\eta_0) = -\frac{1}{3D_1(a=1)}\Phi(\eta_0). \qquad (8.69)$$

The last equality holds here because at very late times, there are no appreciable anisotropic stresses, and $\Phi = -\Psi$.

We may use Eq. (7.7) to express the potential Φ today in terms of the dark matter distribution, so that

$$\Theta_0(\eta_*) + \Psi(\eta_*) \simeq -\frac{\Omega_m H_0^2}{2k^2 D_1(a=1)}\delta(\eta_0). \qquad (8.70)$$

This gives us what we need: an expression for the sum of $\Theta_0 + \Psi$ at recombination that we can plug into the monopole term in Eq. (8.56). To get the anisotropy spectrum today, we then integrate as in Eq. (8.68), leaving

$$C_l^{\text{SW}} \simeq \frac{\Omega_m^2 H_0^4}{2\pi D_1^2(a=1)} \int_0^\infty \frac{dk}{k^2} j_l^2 \left[k(\eta_0 - \eta_*)\right] P(k) \qquad (8.71)$$

where the superscript denotes *Sachs–Wolfe*, in honor of the first people to compute the large-angle anisotropy (Sachs and Wolfe, 1967). The power spectrum is given by Eq. (7.9) with the transfer function set to 1 (since we're considering very large scales). Therefore,

$$C_l^{\text{SW}} \simeq \pi H_0^{1-n} \left(\frac{\Omega_m}{D_1(a=1)}\right)^2 \delta_H^2 \int_0^\infty \frac{dk}{k^{2-n}} j_l^2 \left[k(\eta_0 - \eta_*)\right]. \qquad (8.72)$$

The large-scale anisotropies in Eq. (8.72) can be computed analytically. First, we will use the fact that $\eta_* \ll \eta_0$ and define the dummy variable $x \equiv k\eta_0$. Then the spectrum can be rewritten as

$$C_l^{\mathrm{SW}} \simeq \pi(\eta_0 H_0)^{1-n} \left(\frac{\Omega_m}{D_1(a=1)} \right)^2 \delta_H^2 \int_0^\infty \frac{dx}{x^{2-n}} j_l^2(x). \qquad (8.73)$$

The integral over the spherical Bessel functions can be analytically expressed (Eq. (C.17) from Gradshteyn and Ryzhik, 6.574.2) in terms of gamma functions, leaving

$$C_l^{\mathrm{SW}} \simeq 2^{n-4}\pi^2(\eta_0 H_0)^{1-n} \left(\frac{\Omega_m}{D_1(a=1)} \right)^2 \delta_H^2 \frac{\Gamma\left(l + \frac{n}{2} - \frac{1}{2}\right)}{\Gamma\left(l + \frac{5}{2} - \frac{n}{2}\right)} \frac{\Gamma(3-n)}{\Gamma^2\left(2 - \frac{n}{2}\right)}. \qquad (8.74)$$

If the spectrum is Harrison–Zel'dovich–Peebles, $n = 1$, then the first ratio of the gamma functions $\Gamma(l)/\Gamma(l+2)$ is equal to $[l(l+1)]^{-1}$ using Eq. (C.24). The remaining ratio of gamma functions $\Gamma(2)/\Gamma^2(3/2) = 4/\pi$ using Eq. (C.25), so

$$l(l+1)C_l^{\mathrm{SW}} = \frac{\pi}{2} \left(\frac{\Omega_m}{D_1(a=1)} \right)^2 \delta_H^2, \qquad (8.75)$$

a constant. Indeed, this is the reason why workers in the field typically plot $l(l+1)C_l$: at low l, where the Sachs–Wolfe approximation is a good one, we expect a plateau.

Figure 8.12 shows the COBE measurements of the large-angular-scale anisotropies along with the Boltzmann solutions of three CDM models. Note that, even for $n = 1$, the true spectrum is *not* completely flat as suggested by Eq. (8.75). The dipole at recombination (neglected in Eq. (8.74)) contributes slightly. The integrated Sachs–Wolfe effect also is not completely negligible, especially in the Λ model, wherein the potential starts to decay once the universe becomes Λ-dominated at late times. For an $n = 1$ spectrum, the best fit values of δ_H from COBE are

$$\delta_H = 1.9 \times 10^{-5} \qquad \Omega_m = 1$$

$$\delta_H = 4.6 \times 10^{-5} \qquad \Omega_m = 0.3 \, ; \, \Omega_\Lambda = 0.7. \qquad (8.76)$$

Also shown in Figure 8.12 is a *tilted* model, one in which the primordial spectral index n is not equal to 1. In such models, the anisotropy should scale as l^{n-1} compared with the Harrison–Zel'dovich–Peebles $n = 1$ spectrum. You can see this scaling from Eq. (8.74) or more directly from the integral in Eq. (8.73). The integrand peaks at $x \sim l$, so very roughly every appearence of x there can be replaced by l. The generalization of the integrand from x^{-1} to x^{n-2} therefore leads to a change in the spectrum that scales as l^{n-1}. As indicated in Figure 8.12, the COBE data have the greatest weight at $l \sim 10$, but cover a range of l spanning an order of magnitude. Extreme values of tilt are therefore ruled out by COBE. To get much better constraints on the tilt, though, measurements spanning a larger range of l are necessary.
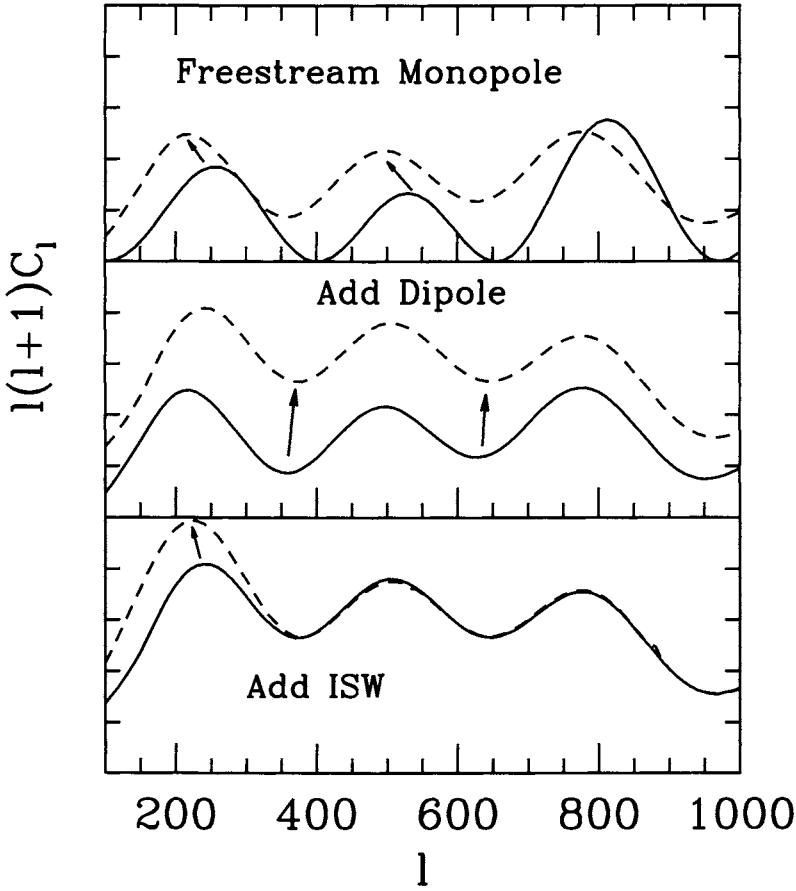
8.6.2 Small Scales

The small-scale anisotropy spectrum depends not only on the monopole, but also on the dipole and the integrated Sachs–Wolfe effect. Figure 8.13 shows all these contributions to the spectrum. Let's consider each in turn.
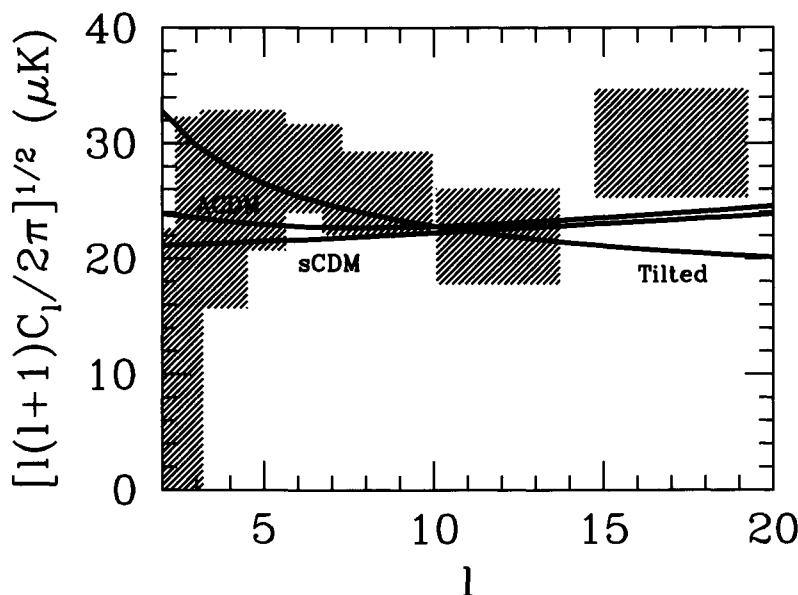
Figure 8.12. Large-scale anisotropies. Hatched boxes show measurements by COBE satellite (Bennett *et al.*, 1996). Curves show the spectra for standard CDM and ΛCDM (both with $n = 1$). The *tilted* model is identical to standard CDM, except $n = 0.5$. The late time integrated Sachs–Wolfe effect enhances anisotropy on the largest scales in ΛCDM. Note that here, and in subsequent C_l figures, the root mean square anisotropy is plotted, proportional to $C_l^{1/2}$. C_l is dimensionless so the units of μK come from multiplying by the present background temperature, $T = 2.73$K.
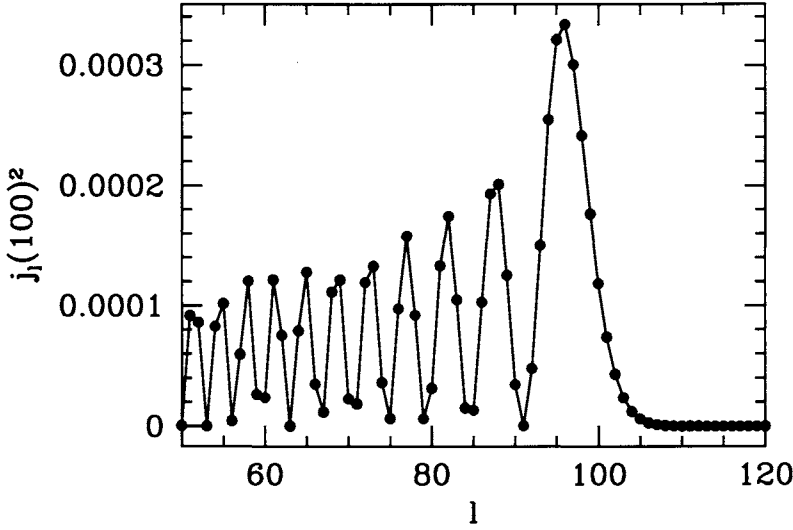
The monopole at recombination $(\Theta_0 + \Psi)(k, \eta_*)$ free-streams to us today, creating anisotropies on angular scales $l \sim k\eta_0$. This is what we expected back in Figure 8.4, showed to be true in Eq. (8.56), and can now see directly in the top panel of Figure 8.13. There are two interesting features of the quantitative aspect of the free-streaming process. First, note that the "zeroes" in the monopole spectrum, here at $400, 650$, and 970, are smoothed out because many modes contribute to anisotropy on a given angular scale. If only the $k = 400/\eta_0$ modes contributed to the anisotropy at $l = 400$, then C_{400} would really be zero. But many nonzero modes, with wavenumber greater than $400/\eta_0$, contribute. These change the zero to a trough in the C_l spectrum.

The second feature of free-streaming worth noticing is that our initial estimate tof the peak positions is not exactly right. Inhomogeneity on scale k does *not* show up as anisotropy precisely on angular scale $l = k\eta_0$. Rather, There is a noticable shift in the top panel, suggesting that a given k-mode contributes to slightly smaller l than we anticipated. This shift arises from the spherical Bessel function in Eq. (8.56). As indicated in Figure 8.14, the peak in the Bessel function comes not when $l = k\eta_0$, but rather at slightly smaller values of l. In addition, our initial

Figure 8.13. Small-scale anisotropy. *Top panel:* The monopole at recombination $(\Theta_0 + \Psi)(k = l/\eta_0, \eta_*)$ contains most of the structure of the final anisotropy spectrum. When free-streamed via the integral in Eq. (8.56), the spectrum shifts slightly to lower l. *Middle panel:* Accounting for the dipole raises the anisotropy spectrum. Since the dipole is out of phase with the monopole, the troughs become less pronounced. *Bottom panel:* The integrated Sachs–Wolfe effect enhances the anisotropy on scales comparable to the horizon. In this case, the potential changes near recombination since the universe is not purely matter dominated then. Thus the first peak gets most of the excess power. Throughout, $h = 0.5, \Omega_b = 0.06, \Omega_m = 1$.

estimate for the location of the peaks in k-space, Eq. (8.25), is also slightly high. For example, the expected position of the first peak, $\pi\eta_0/r_s$, for the model depicted in Figure 8.13 is a little over 280. The first peak in the monopole in k-space, however, appears at $k\eta_0 \sim 260$. These two effects — fixed k projects to slightly smaller l and peaks on slightly larger scales than expected from Eq. (8.25) — serve to move the predicted positions of the peaks to lower l. A better approximation for the first

Figure 8.14. The spherical Bessel function, $j_l(100)$. Note that the peak occurs at $l \simeq 90$, slightly smaller than the argument.

peak position is $l_p \simeq 0.75\pi\eta_0/r_s$.

The dipole at recombination is smaller than the monopole and out of phase with it. The middle panel in Figure 8.13 shows that adding in the dipole raises the overall anisotropy level, but particularly fills in the troughs. Without the dipole (in this model) the ratio of the height of the first peak (at $l \sim 200$) to the height of the first trough (at $l \sim 400$) is about 2.5:1; the dipole lowers this ratio to 1.5:1. This is a direct manifestation of the dipole and monopole being out of phase with one another. That is, at the places where the monopole contributes least to the anisotropies, at its troughs, the dipole contributes the most. One other comment about the relation between the monopole and the dipole: they add incoherently. By incoherently, I mean that the cross term of Θ_l from the monopole multiplied by Θ_l from the dipole vanishes when integrating over all k-modes to get the C_l's. This can be seen mathematically from the properties of the spherical Bessel function (Exercise 12). Incoherence implies that the dipole is not as important in the power spectrum as one might naively think. If the amplitude of the dipole is 30% of that of the monopole at recombination, the dipole's contribution to the C_l's is only 10% ($1^2 + 0.3^2 = 1.1$).

The integrated Sachs–Wolfe effect is also important if the potential changes after recombination. To see which scales are affected by the ISW effect, consider the integral in Eq. (8.56). Suppose the potential changes at time η_c, with all sub-horizon scales ($k\eta_c > 1$) being affected. The Bessel function peaks at $l \sim k(\eta_0 - \eta_c)$; so all angular scales $l > (\eta_0 - \eta_c)/\eta_c$ are affected. The largest effect is typically at the horizon.

The best, and most prevalent, example of the ISW effect is that due to residual

radiation at recombination. If the universe were purely matter dominated, there would be no such effect. But, the transition to pure matter domination is not abrupt, and even for $a_{\text{eq}} \sim 10^{-4}$, an ISW effect occurs right after recombination. This early ISW effect is particularly important because it adds coherently with the monopole. To see this, integrate the last term in Eq. (8.56) by parts. Then, the dominant contribution comes from $\eta \simeq \eta_*$, so the Bessel function can be evaluated there, leaving the trivial integral which gives

$$\Theta_l(k,\eta_0)^{\text{early ISW}} = [\Psi(k,\eta_0) - \Psi(k,\eta_*) - \Phi(k,\eta_0) + \Phi(k,\eta_*)]\, j_l\,[k(\eta_0 - \eta_*)].$$
$$(8.77)$$

This adds exactly in phase with the monopole (which is proportional to the same Bessel function) so even though the magnitude of the effect on Θ_l is much smaller than is the dipole, the effect on the anisotropy spectrum is disproportionate. A 30% dipole leads to a 10% shift in the C_l's, while a 5% ISW effect leads to the same 10% shift in the C_l's. The bottom panel shows that the large scales, those with $l \sim \eta_0/\eta_*$, get a big boost from this early ISW effect.

8.7 COSMOLOGICAL PARAMETERS

The anisotropy spectrum depends on cosmological parameters. This fundamental realization initially caused great consternation ("We will never be able to measure any one parameter because there is too much degeneracy"). As more quantitative studies were carried out, the pendulum swung to the other side ("We will be able to disentangle the degeneracies and measure cosmological parameters to percent accuracy"). More recently, the community has settled into a state of cautious optimism. Indeed, just a decade after the initial discovery of large scale anisotropies by COBE, there were a host of experiments which together seemed to pin down one parameter (the total energy density) by measuring the location of the first peak. Several of these had measured the subsequent two peaks, allowing an inference of the baryon density, the parameter which most affects the heights and locations of these peaks.

We now have developed the theoretical tools needed to participate in the parameter determination discussion. In this section, we apply these tools to understand how the anisotropy spectrum varies as cosmological parameters vary.

One very important decision that must be made is which parameters will be allowed to vary. I will consider eight parameters:

- Curvature density, $\Omega_k \equiv 1 - \Omega_m - \Omega_\Lambda$
- Normalization, C_{10}
- Primordial tilt, n
- Tensor modes, r (for a precise definition, see Exercise 18)
- Reionization, parametrized by τ back to recombination
- Baryon density, $\Omega_b h^2$
- Matter density, $\Omega_m h^2$
- Cosmological constant energy density, Ω_Λ

There are two aspects of this list worth stressing. The first is that obviously it does not include all possible cosmological parameters. Some favorites missing are a neutrino mass (I will set all masses to zero in the following), the equation of state for dark energy w (will be fixed at -1 corresponding to a cosmological constant), and tensor tilt n_T (fixed at zero). The second important point is that I have deliberately chosen very specific combinations of these parameters, e.g., $\Omega_b h^2$, not Ω_b and h separately. While there is good reason for this (e.g., the alternating peaks effect depends on $\Omega_b h^2$), it also is a source of confusion. A common complaint is that, within the context of a flat universe (the first parameter, the curvature density, equal to zero), why should both the cosmological constant and the matter density be allowed to vary? Mustn't their sum equal 1? It is true that $\Omega_m + \Omega_\Lambda$ must equal 1 in a flat universe. But that does not preclude us from varying both $\Omega_m h^2$ and Ω_Λ, since h can change while the sum of the two densities is 1.

To harp on this point, consider two analysts. Analyst A works in the context of a flat universe and uses $\Omega_m h^2$ and Ω_Λ as her two free parameters. Analyst B also assumes the universe is flat, but takes h and Ω_Λ as his two parameters. When A raises Ω_Λ, the matter density ($\Omega_m h^2$) is kept fixed, so the epoch of equality is kept fixed. However, when analyst B raises his Ω_Λ, to keep the universe flat, he must lower Ω_m. He is therefore also lowering the matter density (since h is kept fixed), thereby moving $a_{\rm eq}$ closer to today. That change in $a_{\rm eq}$ will lead to an enhanced ISW effect, and therefore a larger first peak. Analyst A, who had the foresight to separate out this effect by choosing $\Omega_m h^2$ as one of her parameters, sees no such enhancement. And, indeed the enhancement is caused only indirectly by Ω_Λ: rather it is the direct result of a smaller $\Omega_m h^2$.

Let's now consider the effect of each parameter in turn.

8.7.1 Curvature

If the universe is not flat, then the simple picture of Figure 8.4 is no longer accurate since the geodesics of massless particles are such that photons starting out parallel to each other slowly diverge. Consider the implication of this divergence for anisotropies. Suppose the identical pattern of inhomogeneities was in place at recombination in both a flat and open universe. As shown in Figure 8.15, the physical scale with maximal anisotropy (the first peak) gets projected onto a much smaller angular scale in an open universe. The peaks should therefore be shifted to higher l. As shown in Figure 8.16, this is precisely what happens.

The magnitude of this effect is determined by the comoving angular diameter distance to the last scattering surface, in a flat universe simply equal to $\eta_0 - \eta_*$, and in a universe with curvature given by Eq. (2.46) out to z_*. Figure 8.17 shows this distance as a function of the curvature density with all other parameters held fixed. The angular diameter distance scales as $(1 - \Omega_k)^{-0.45}$, so that it is a factor of 1.7 larger in an open $\Omega_k = 0.7$ universe than in a flat universe. Notice from Figure 8.16 that this is precisely the factor by which the first peak shifts from one model to
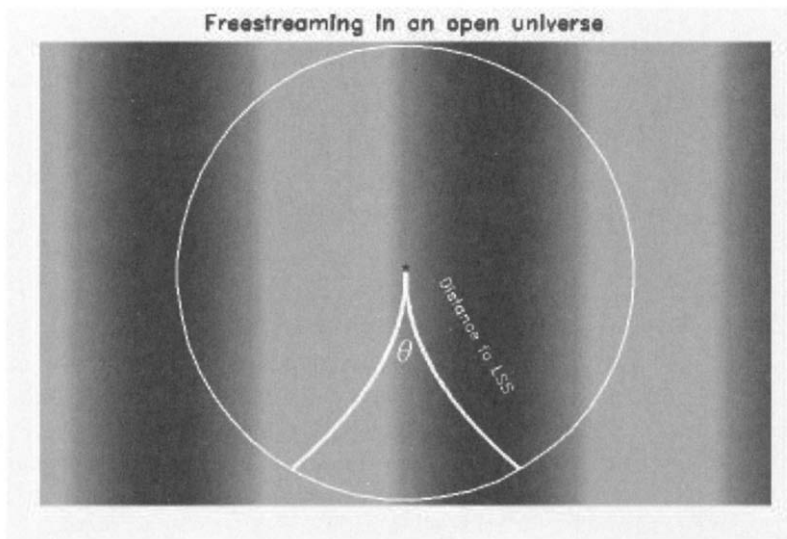
Figure 8.15. Photon trajectories in an open universe diverge. Perturbations at last scattering turn up on smaller scales in an open universe than they do in a flat universe.

the other. Of all the parameters under consideration, curvature by far causes the largest shift in the location of the peaks.

Figure 8.16 also shows data circa 2002. There is a clear rise up to a first peak at $l \sim 200$ and an equally clear fall past this first peak. When the data first started coming in (around 1998), a skeptic could plausibly claim that no one data set spanned the whole peak, and it is difficult to combine data sets. Within a year or two, though, this objection vanished as larger data sets such as TOCO (Miller *et al.*, 1999), Boomerang (de Bernardis *et al.*, 2000), and Maxima (Hanany *et al.*, 2000) all contained enough information by themselves to rule out an open universe. The DASI detection (Halverson *et al.*, 2002), together with the reanalyzed Boomerang and Maxima data, cemented the case for a flat universe.

Of course, a truly flat universe is only one point in parameter space, the point at which the sum of the energy densities exactly equals the critical density, and no data will ever rule out all values except for this one point. Rather, the data now suggest that the total density is equal to the critical density with an error of about 5%. The classic open universe once favored by astronomers had 30% of the critical density, and so is ruled out with very high confidence.

8.7.2 Degenerate Parameters

Figure 8.18 shows the results of varying four parameters. Before considering each in turn, it is important to state the obvious. All of these parameters change the spectrum in very similar ways. The shape of the spectrum varies hardly at all; rather, these parameters simply move the spectrum up and down.
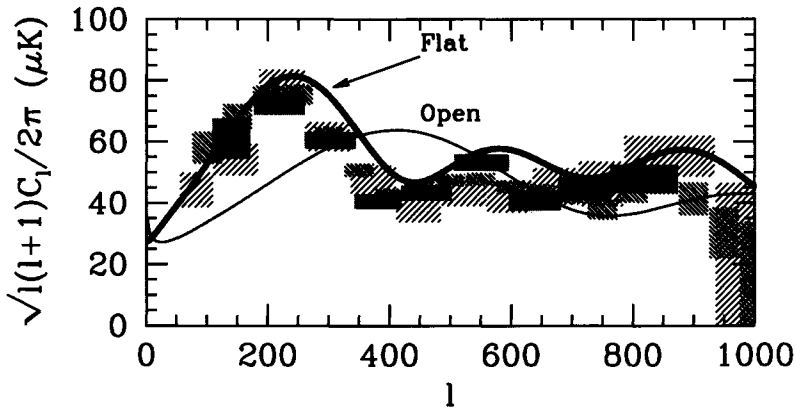
Figure 8.16. The anisotropy spectrum in flat versus open universe. Also shown are data from three small-scale experiments: DASI (darkest; Halverson *et al.*, 2002), Boomerang (medium; Netterfield *et al.*, 2002), and Maxima (lightest; Lee *et al.*, 2001). The pattern of peaks and troughs persists in the open universe but is shifted to smaller scales. The data clearly favor the flat case. Both curves have identical parameters $n = 1, \Omega_m h^2 = 0.15, \Omega_b h^2 = 0.02$ with no reionization, tensors, or cosmological constant. *Open* curve has $\Omega_k = 1 - \Omega_m = 0.7$; *flat* has the same parameters except $\Omega_k = 0$.
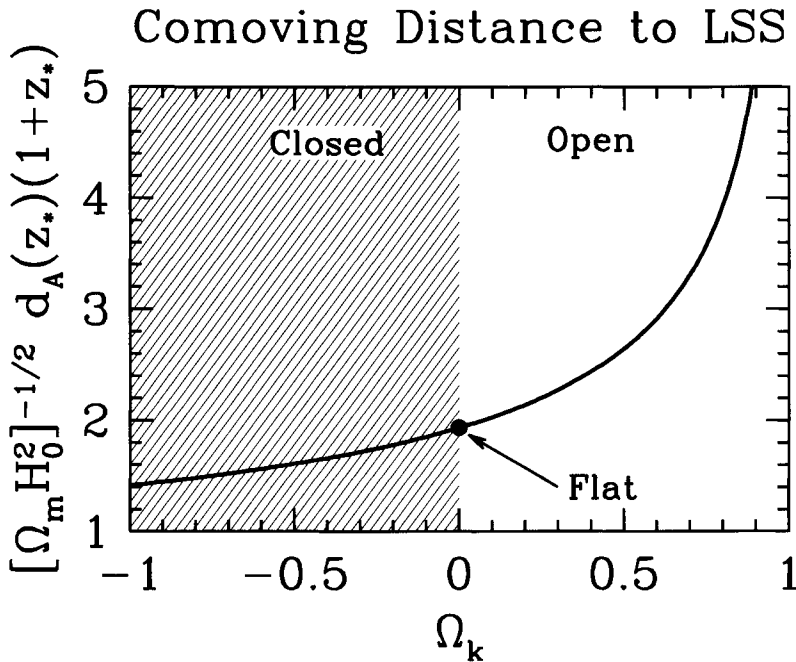
Figure 8.17. Comoving angular diameter distance back to the last scattering surface at $z_* \simeq 1100$ as a function of curvature. The distance is larger in an open universe than in a closed universe.
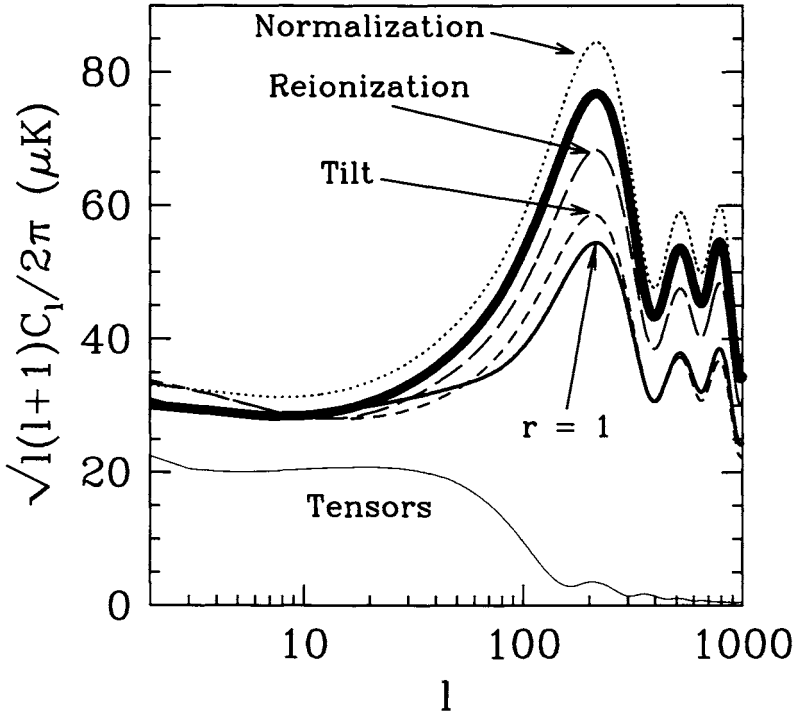
Figure 8.18. Changes in the anisotropy spectrum as C_{10}, τ, r, and n vary. The base model (thick curve) is a flat universe with no reionization or tensors, $n = 1$, $\Omega_m h^2 = 0.16$, $\Omega_b h^2 = 0.021$, and $\Omega_\Lambda = 0.7$. The thin curves vary one parameter each. *Reionization* corresponds to letting the optical depth back to the last scattering surface equal 0.2 instead of zero; *tilt* has a primordial spectum with $n = 0.8$; $r = 1$ has an equal contribution of scalars and tensors to the quadrupole; and *normalization* has C_{10} 10% higher than the base model. The curve labeled *tensors* is the contribution to the anisotropy from tensors only. Only the $r = 1$ curve includes this contribution; all others assume no anisotropy from tensors.

Normalization. The parameter C_{10} trivially moves the spectrum up or down. Note that, of the four parameters varied in Figure 8.18, it is the only one which can raise the amplitude of the spectrum.

Tilt. We have already considered the large-angle effects of a tilted ($n \neq 1$) spectrum. If $n < 1$, then the small-scale anisotropies are smaller than in the $n = 1$ model. Figure 8.18 shows that, as smaller and smaller scales are probed, the effect becomes more pronounced. So of the four parameters considered here, tilt has the most distinctive shape — it is not a simple up–down shift — and perhaps will be most easily extracted. Quantitatively, the spectrum scales as

$$\frac{C_l(n)}{C_l(n=1)} \simeq \left(\frac{l}{l_{\text{pivot}}}\right)^{n-1} \tag{8.78}$$

where here $l_{\mathrm{pivot}} = 10$ since we are fixing C_{10}. Accounting for the fact that $\sqrt{C_l}$ is plotted in Figure 8.18, we see from the point at $l = 1000$ that this scaling works extremely well.

Reionization. The universe was almost certainly reionized at late times. We see this in the absorption spectra of high-redshift quasars, where no evidence is seen of a uniform background of neutral hydrogen until we go back as least as far as $z \sim 6$ (Becker *et al.*, 2001; Fan *et al.*, 2002). Reionization brings the CMB back in contact with electrons. If enough scattering takes place, that is, if the optical depth back to the last scattering surface is high enough, isotropy is restored; equivalently, primordial anisotropies are washed out.

There are several ways to see the effect of reionization quantitatively. One is to imagine a photon traveling in our direction with temperature $T[1 + \Theta]$, where T is the background temperature and Θ is the perturbation for which we have solved. If these photons hit a region with optical depth τ, only a fraction $e^{-\tau}$ will escape and continue on their way to us. In addition to these, we will also get a fraction $1 - e^{-\tau}$ from the ionized region. All of these have the equilibrated temperature, T. So the temperature we see today is

$$T[1 + \Theta]e^{-\tau} + T\left(1 - e^{-\tau}\right) = T\left[1 + \Theta e^{-\tau}\right]. \qquad (8.79)$$

Subtracting from this the mean temperature T tells us that the fractional anisotropy will be Θ, the primordial one set up at $z \simeq 1100$, multiplied by $e^{-\tau}$. Of course this argument can affect only those scales within the horizon at the time of reionization, so multipoles l larger than $\eta_0/\eta_{\mathrm{reion}}$ will be suppressed by $e^{-\tau}$; small l will be unaffected. This is seen in Figure 8.18, where the reionization curve falls on top of the base model on large scales but is uniformly suppressed on small scales.

Tensors. We saw in Chapter 5 that once they enter the horizon, the amplitude of gravitational waves dies away. Therefore, gravity waves affect the anisotropy spectrum only on scales larger than the horizon at recombination. Typically, this translates into angular scales $l < 100$. Indeed the *tensors* curve in Figure 8.18 shows that tensors die out after $l > 100$. We can observe only the sum of anisotropies due to tensors and scalars. So if tensor perturbations were produced during inflation, and if the total (scalar plus tensor) anisotropy spectrum is fit to the large-scale (COBE) data, then the small-scale scalar amplitude is smaller than it would otherwise be. Therefore, on scales $l > 100$ where only scalars remain, the anisotropy spectrum is identical to the base model in Figure 8.18, but with a lower amplitude.

8.7.3 Distinct Imprints

The final variations we will consider are changes in the baryon density $\Omega_b h^2$, the matter density $\Omega_m h^2$, and the cosmological constant. As can be seen from Figure 8.19, these changes lead to richer variations in the anisotropy spectrum; as such they are somewhat harder to understand (but easier to extract from the data!) than the parameters in the previous subsection.
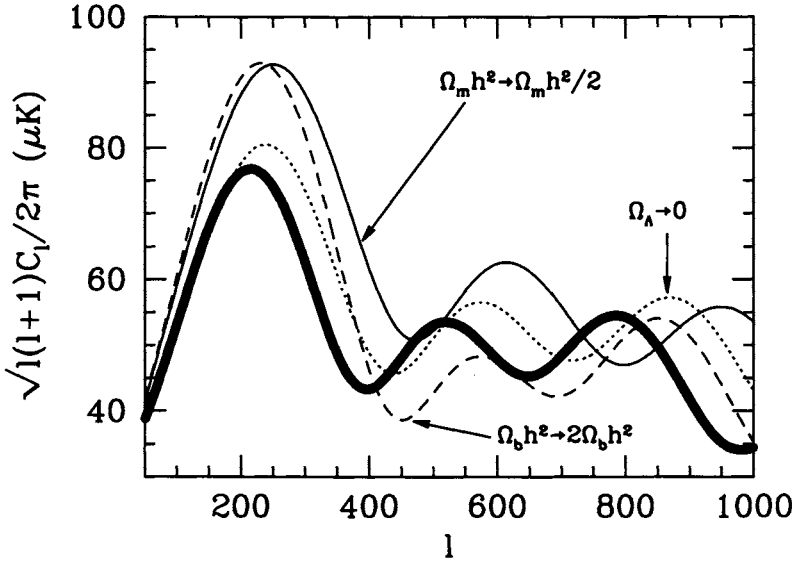
Figure 8.19. Changes in the anisotropy spectrum as baryon density, matter density, and cosmological constant vary. Same base model as Figure 8.18.

Each of these parameters induces a small shift in the locations of the peaks and troughs in the spectrum. To understand these shifts, it is important to recall that since inhomogenities on scales k show up at $l = k\eta_0$ in a flat universe, the peaks in a flat universe will show up at $l_p \simeq k_p\eta_0 \simeq n\pi\eta_0/r_s(\eta_*)$ (Eq. (8.25), but also see the discussion on page 247 that argues that the actual value of l_p is $\sim 25\%$ lower). Figure 8.20 shows this ratio as a function of matter and baryon density. It is more sensitive to the matter density, so the peak spacing increases as the matter density goes down. But there is also a little sensitivity to the baryon density. With the densities fixed, introducing a cosmological constant does not change the sound horizon, but it does slightly affect η_0, so the peaks shift in that cases as well.

Baryon density. In addition to the lateral shift in the spectrum due to the change in the sound horizon, changes in the baryon density affect the heights of the peaks as well. We have already touched on the ways in which the anisotropy spectrum depends on the baryon density. The foremost, clearly visible in Figure 8.19, is that odd peaks (first and third in the figure) are higher than the even peaks when the baryon density is large. This is a direct ramification of the lower frequency of oscillations due to the massive baryons. This change is virtually unique, making the baryon density one of the easiest parameters to extract from the CMB. Observations as of 2001 (e.g., Pryke et al., 2001) pin down $\Omega_b h^2 = 0.022\pm0.04$, and this constraint will undoubtedly get tighter with data from the Map and Planck satellites. The second change due to $\Omega_b h^2$ is that an increased baryon density reduces the diffusion length. Therefore, a larger baryon density means damping moves to smaller angular scales, so the anisotropy spectrum on scales $l > 1000$ is larger in a high-$\Omega_b h^2$ model.
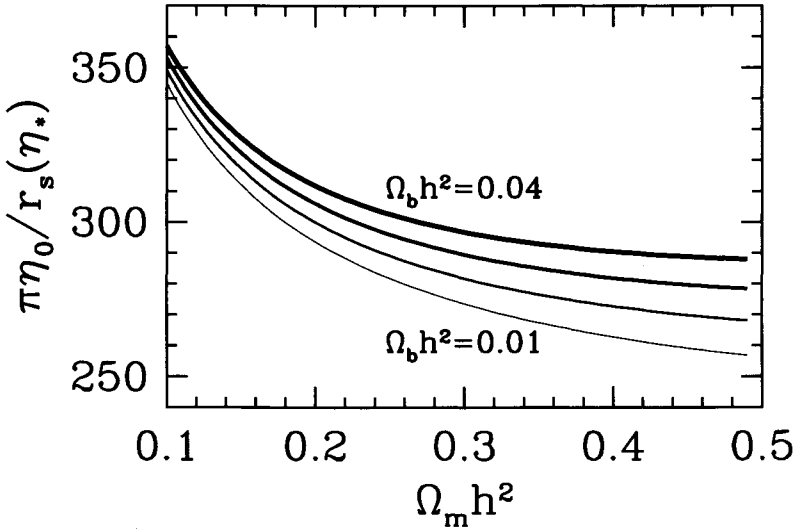
Figure 8.20. The inverse sound horizon at recombination. In a flat universe, the spacing between the acoustic peaks in the CMB is equal to $\pi\eta_0/r_s(\eta_*)$.

Cosmological constant. The cosmological constant is a late-time phenomenon. It was not around at recombination, and therefore could not have affected perturbations then. Therefore, the only possible effects of a cosmological constant are on free-streaming and on the largest angular scales just entering the horizon at recent times. The change due to free-streaming is evident in Figure 8.19. The spectrum is shifted to smaller angular scales if there is no cosmological constant. You will show in Exercise 13 that this small shift can be readily explained by comparing the conformal times in a Λ universe and a matter-dominated universe. Figure 8.19 also shows that the anisotropy spectrum is slightly lower on small scales in a Λ universe. This is a direct result of the large-angle normalization. In a Λ universe, there is a late-time ISW effect, which enhances the anisotropies on large angles. If we normalize on these scales, then the small-scale anisotropy gets correspondingly smaller.

Matter density. If the matter density is low, the epoch of equality occurred closer to recombination, so that the radiation density must be accounted for in computing the inhomogeneities at recombination. In particular, the decaying potential due to the inability of the radiation to cluster provides a strong driving force for the oscillations. Therefore, $\Theta_0(\eta_*)$ is larger than in a purely matter-dominated universe. Further, after recombination, since the potential is not constant, the ISW effect also contributes significantly to the final anisotropy spectrum. Therefore, the small-scale anisotropies increase if the matter density is low. This effect too has apparently been detected, with measurements (Pryke *et al.*, 2001) implying $\Omega_m h^2 = 0.16 \pm 0.04$.

SUGGESTED READING

The large-scale Sachs–Wolfe effect was first predicted by Sachs and Wolfe (1967), just several years after the discovery of the CMB. Several groups initiated the study of anisotropies in the tightly coupled limit: Doroshkevich, Zel'dovich, and Sunyaev (1978), Atrio-Barandela and Doroshkevich (1994), and Jorgenson *et al.* (1995). The approach was perfected by Seljak (1994) and Hu and Sugiyama (1995), the latter of which is the basis for the semianalytic treatment of this chapter. Again, CMBFAST described in Seljak and Zaldarriaga (1996) is a crucial tool for fast, accurate numerical work. Diffusion damping is sometimes called *Silk* damping because of the Silk (1968) paper recognizing its importance. Two other papers of interest are Zaldarriaga and Harari (1995) which discusses the effect of polarization on the damping scale (see Exercise 7) and Hu and White (1997a) which, among other things, gives fits to the damping scale valid for a wide range of parameters.

The question of how the anisotropy spectrum depends on cosmological parameters has been explored in literally hundreds of papers over the past decade. I remember Dick Bond, one of the pioneers in the field, giving a talk in 1992 at a conference about the early COBE data waving his hands through an invisible multidimensional parameter space, explaining that our goal now was to navigate through this space. Among the most important realizations were the dependence on curvature (Kamionkowski, Spergel, and Sugiyama 1994), the degeneracy of the height of the first peak (Bond *et al.*, 1994), and breaking of this degeneracy by smaller scale information (Jungman *et al.*, 1995). More recently, Hu *et al.* (2000) is a good reference.

I have given short shrift (or no shrift) to some important parameters. The effect of dark energy on the CMB has now been well studied: first by Coble, Dodelson, and Frieman (1997) and then more generally by Caldwell, Dave, and Steinhardt (1998). Massive neutrinos affect the anisotropy spectrum at the 5-10% level (Ma and Bertschinger, 1995 and Dodelson, Gates and Stebbins, 1996). The anisotropies due to tensors became a hot topic after the COBE discovery. For a semianalytic treatment and references to the dozens of papers relating the tensor anisotropy to parameters in the potential, see Turner, White and Lidsey (1993). Although the effect of reionization on the primary anisotropies generated before recombination is well understood, a hot topic now is *secondary* anisotropies, those generated after reionization. These will likely be probed by the next generation of experiments.

3K: The Cosmic Microwave Background (Partridge) is a good introduction to some of the experimental issues I have neglected in this book. The COBE discovery paper is Smoot *et al.* (1992) with the 4-year observations presented in Bennett *et al.* (1996). There were many good analyses papers written on the COBE data; I've relied on Bunn and White (1997), which is especially good for using COBE to normalize the matter power spectrum, and Tegmark (1997), from which the points in Figure 8.12 are taken. The two satellite experiments are Map (http://map.gsfc.nasa.gov) and Planck (http://sci.esa.int/planck/). Map was launched in 2001, and Planck is scheduled to be launched in 2007.

EXERCISES

Exercise 1. Most of this book is devoted to understanding adiabatic perturbations with the initial conditions derived in Chapter 6. Another class of perturbations are *isocurvature* perturbations with initial conditions $\Theta_0 = \Psi = \Phi = 0$. Show that these initial conditions imply that

$$\Theta_0(\eta_*) + \Psi(\eta_*) = 2\Psi(\eta_*). \tag{8.80}$$

Exercise 2. The equation for a damped harmonic oscillator is

$$m\ddot{x} + b\dot{x} + kx = 0. \tag{8.81}$$

Find the solutions to this equation if $k/m > (b/2m)^2$. What is the frequency of oscillations? How does this differ from the undamped $(b = 0)$ solution? What is the other effect of nonzero b besides the change in frequency?

Exercise 3. Determine $R(\eta_*)$ when $\Omega_b h^2 = 0.01, 0.02$. Plot the sound speed as a function of the scale factor for these two values of $\Omega_b h^2$.

Exercise 4. Show that the sound horizon can be expressed in terms of the conformal time as

$$r_s(\eta) = \frac{2}{3k_{\rm eq}}\sqrt{\frac{6}{R(\eta_{\rm eq})}} \ln\left\{\frac{\sqrt{1+R} + \sqrt{R + R(\eta_{\rm eq})}}{1 + \sqrt{R(\eta_{\rm eq})}}\right\}, \tag{8.82}$$

where $k_{\rm eq}$ is given in Eq. (7.39).

Exercise 5. Obtain the WKB solution to Eq. (8.18). Write

$$\Theta_0 = Ae^{iB} \tag{8.83}$$

with A and B real. Show that the homogeneous part of Eq. (8.18) breaks up into two equations, coming from the real and imaginary part:

$$\text{Real}: -(\dot{B})^2 + \frac{\ddot{A}}{A} + \frac{\dot{R}}{1+R}\frac{\dot{A}}{A} + k^2 c_s^2 = 0 \tag{8.84}$$

$$\text{Imaginary}: 2\dot{B}\frac{\dot{A}}{A} + \ddot{B} + \frac{\dot{R}}{1+R}\dot{B} = 0. \tag{8.85}$$

Find B using the real part and the fact that B changes much more rapidly than A. Then, use the imaginary equation to determine A. Show that the homogeneous solutions obtained in this way differ from the simple oscillatory solutions of Eq. (8.21) by a factor of $(1 + R)^{1/4}$.

Exercise 6. Obtain a semianalytic solution for $\Theta_0 + \Psi$ and Θ_1 at recombination by carrying out the integrals in Eqs. (8.24) and (8.26). To do this you will need expressions for the gravitational potentials. Hu and Sugiyama (1995) provided the following convenient fits:

$$\Phi(k,y) = \bar{\Phi}(k,y)\left\{[1 - T(k)]\exp[-0.11(ky/k_{\text{eq}})^{1.6}] + T(k)\right\}$$

$$\Psi(k,y) = \bar{\Psi}(k,y)\left\{[1 - T(k)]\exp[-0.097(ky/k_{\text{eq}})^{1.6}] + T(k)\right\}$$

where $y \equiv a/a_{\text{eq}}$, $T(k)$ is the BBKS transfer function and the large-scale potentials are

$$\bar{\Phi}(k,y) = \frac{3}{4}\left(\frac{k_{\text{eq}}}{k}\right)^2 \frac{y+1}{y^2}\Delta_T(y)$$

$$\bar{\Psi}(k,y) = -\frac{3}{4}\left(\frac{k_{\text{eq}}}{k}\right)^2 \frac{y+1}{y^2}\left(\Delta_T(y) + 0.65N_2/(1+y)\right). \tag{8.86}$$

Finally the two functions N_2 and Δ_T are

$$N_2(y) = -0.1\frac{20y+19}{3y+4}\frac{y^2}{y+1}\Phi_{ls} - \frac{8}{3}\frac{y}{3y+4} + \frac{8}{9}\ln[3y/4 + 1]$$

$$\Delta_T = \left[1.16 - \frac{0.48y}{y+1}\right]\Phi_{ls}\frac{y^2}{y+1}. \tag{8.87}$$

Here Φ_{ls} is the large-scale solution of Eq. (7.32).

Exercise 7. Our treatment of diffusion damping neglected the effect of polarization. Go through the same expansion in $\dot{\tau}^{-1}$ that we carried out in Section 8.4 this time accounting for polarization. Show that this changes the factor of $8/9$ in Eq. (8.40) to $16/15$. This beautiful result was obtained by Zaldarriaga and Harari (1996) when the first author was an undergraduate!

Exercise 8. Assume that all electrons associated with hydrogen stay ionized and set $R = 0$. Evaluate the damping scale, k_D, defined in Eq. (8.40). Show that in this limit, the damping scale is given by Eq. (8.42), where

$$f_D(y) = 5\sqrt{1+1/y} - \frac{20}{3}(1+1/y)^{3/2} + \frac{8}{3}\left[\left(1+1/y\right)^{5/2} - 1/y^{5/2}\right]. \tag{8.88}$$

Exercise 9. Show that

$$\int d\Omega\, Y_{lm}(\hat{p})\mathcal{P}_l(\hat{p}\cdot\hat{k}) = \frac{4\pi}{2l+1}. \tag{8.89}$$

Exercise 10. There is a different way to go from the inhomogeneous temperature field at recombination, $\Theta_0(\vec{x}, \eta_*)$ or $\Theta_0(\vec{k}, \eta_*)$, to the anisotropy pattern today, a_{lm}, than that given in the text.

(a) Assume that the photons we see today from direction $\hat{p}$ come from the surface of last scattering: $\Theta(\vec{x}_0, \hat{p}, \eta_0) = (\Theta_0 + \Psi)(\vec{x} = \chi_* \hat{p}, \eta_*)$ where x_0 is our position. Fourier transform the right-hand side and expand the left in terms of spherical harmonics to get

$$\sum_{lm} a_{lm} Y_{lm}(\hat{p}) = \int \frac{d^3k}{(2\pi)^3} \, e^{i\vec{k}\cdot\hat{p}\chi_*} (\tilde{\Theta} + \tilde{\Psi})(\vec{k}, \eta_*). \tag{8.90}$$

Now expand the exponential using Eq. (C.16) and then expand the resulting Legendre polynomial using Eq. (C.12). Equate the coefficients of $Y_{lm}(\hat{p})$ to get an expression for a_{lm}.

(b) Square the a_{lm} you got in **(a)** and take the expectation value to get an expression for C_l. You should recapture the expression in Eq. (8.68) with Θ_l given by the first term in Eq. (8.56).

Exercise 11. A simple way to estimate the COBE normalization of δ_H is to fix C_{10}. From Figure 8.12, estimate C_{10}. Use this and the Sachs–Wolfe formula, Eq. (8.75), to estimate δ_H for a flat, matter-dominated universe. Compare with the number given in Eq. (8.76).

Exercise 12. Show that the cross-terms from the monopole and dipole vanish when summing over all modes. The monopole is proportional to $j_l(k\eta_0)$ while the dipole is proportional to $j_l'(k\eta_0)$. Compute the three possible integrals

$$\int_0^\infty dx\, j_l j_l \quad ; \quad \int_0^\infty dx\, j_l j_l' \quad ; \quad \int_0^\infty dx\, j_l' j_l'. \tag{8.91}$$

Show that the integrals of the squares (j_l^2 and $(j_l')^2$) are much larger than the integral of the cross-term $j_l j_l'$. Do the integrals for $l = 10$ up to $l = 50$.

Exercise 13. Determine the shift in the locations of the peaks and troughs in the CMB anisotropy spectrum if the universe is flat with a cosmological constant as opposed to flat and matter dominated. Keep the sound horizon fixed in this calculation by fixing $\Omega_m h^2 = 0.15$. The peak positions then depend only on the distance to the last scattering surface, $\eta_0 - \eta_*$. Consider two flat models: (i) $\Omega_\Lambda = 0$ (so that $\Omega_m = 1$) and (ii) $\Omega_\Lambda = 0.7$ (so that $\Omega_m = 0.3$). What value of h is needed in the two cases to keep $\Omega_m h^2$ fixed? Determine $\eta_0 - \eta_*$ in each case (in the the cosmological constant case, you will have to do the integral numerically). Compare your result with the fitting formula: $\eta_0 \propto 1 + \ln(\Omega_m^{0.085})$ and with the shift in Figure 8.19.

Exercise 14. Compute the conformal time today in a flat model with dark energy $\Omega_{\rm de} = 0.7$ today with $w = -0.5$. Compare the expected shift in the anisotropy spectrum with the cosmological constant model of the previous problem.

Exercise 15. Determine the effects of reionization using the Boltzmann equation. Neglect the gravitational potentials, the velocity, and Θ_0 in the Boltzmann equation for photons. Start with a spectrum $\Theta_l(\eta)$ and evolve till today. Show that the moments are indeed suppressed by $e^{-\tau}$.

Exercise 16. Assume that recombination took place instantaneously. Show that the solution for the lth moment due to tensor perturbations (Eq. (4.116)) is

$$\Theta_l^T = -\frac{1}{2} \int_{\eta_*}^{\eta_0} d\eta \ \dot{h} \ j_l[k(\eta_0 - \eta)]. \tag{8.92}$$

Exercise 17. Using the decomposition for tensor modes given in Eq. (4.115), find the contribution to the C_l's from $\Theta_l^T(k)$. That is, show that the analogue of Eq. (8.68) for tensors is

$$C_{l,i}^T = \frac{(l-1)l(l+1)(l+2)}{\pi} \int_0^\infty dk \ k^2$$

$$\times \left| \frac{\Theta_{l-2,i}^T}{(2l-1)(2l+1)} + 2 \frac{\Theta_{l,i}^T}{(2l-1)(2l+3)} + \frac{\Theta_{l+2,i}^T}{(2l+1)(2l+3)} \right|^2, \tag{8.93}$$

where i denotes the two different components $+$ and $\times$.

Exercise 18. Determine the spectrum of anisotropies due to gravity waves produced during inflation.
(a) Combine the results of the previous two problems, your solution to Exercise 5.12, and the primordial amplitude of gravity waves in Eq. (6.100) to find the large-angle C_l's due to inflation-produced gravity waves.
(b) Tensor anisotropies are often parametrized by

$$r \equiv \frac{C_2^T}{C_2^S} \tag{8.94}$$

where C_2^T is the variance of the quadrupole due to tensors and C^S is the same due to scalars.[8] We already derived an expression for the scalar C_2 in Eq. (8.75). Find C_2^T and compute r to first order in the slow roll parameter ϵ.
(c) The results of part (b) and Eq. (6.104) imply a *consistency relation* – a robust prediction of inflation – between the two observables n_T and r. What is the consistency relation?

---

[8]Note that this convention is not universal; r is sometimes defined to the (more precisely constrained) ratio at $l \sim 10$.